

Quantum Coherence and Energy Landscapes in Photosynthetic Systems
Investigated with Two-Dimensional Electronic Spectroscopy

by

Tessa Rae Calhoun

A dissertation submitted in partial satisfaction of the

requirements for the degree of

Doctor of Philosophy

in

Chemistry

in the

Graduate Division

of the

University of California, Berkeley

Committee in charge:

Professor Graham R. Fleming, Chair

Professor Richard J. Saykally

Professor Krishna K. Niyogi

Fall 2010

Quantum Coherence and Energy Landscapes in Photosynthetic Systems
Investigated with Two-Dimensional Electronic Spectroscopy

Copyright 2010

by

Tessa Rae Calhoun

Abstract

Quantum Coherence and Energy Landscapes in Photosynthetic Systems
Investigated with Two-Dimensional Electronic Spectroscopy

by

Tessa Rae Calhoun

Doctor of Philosophy in Chemistry

University of California, Berkeley

Professor Graham R. Fleming, Chair

Two-dimensional (2D) electronic spectroscopy has recently emerged as a powerful technique for the study of complex photodynamics in a variety of condensed phase systems. The application of this technique to both photosynthetic pigment-protein complexes and chromophore solutions has provided insight into their intricate excitation energy transfer mechanisms and landscapes. Analysis of beating peak amplitudes in 2D spectra of the Fenna-Matthews-Olson bacteriochlorophyll complex combined with changing lineshapes has revealed signals consistent with excitonic coherence. In addition, the long lifetime of the coherence indicates a reversible, wavelike motion of energy through the complex as opposed to the classical hopping picture. This quantum-mechanical behavior may explain the near unity quantum efficiency of excitation energy transfer observed in networks of photosynthetic complexes. The inclusion of a noncollinear optical parametric amplifier producing broad bandwidth pulses enables the exploration of excitonic coherence in Light Harvesting Complex II, the most abundant antenna complex in higher plants. Long-lived quantum coherence is again observed suggesting this to be a universal phenomenon in natural photosynthetic systems. To expand upon these findings, a coherence power spectrum is produced. This novel technique allows the first direct experimental determination of the excitonic energy levels. In another set of experiments, the building an adaptive, pulse-shaping apparatus allows optimal compression of the broad bandwidth pulses for use in probing the debated electronic structure of β -carotene. Oscillating lineshapes reveal coupling of electronic states to high energy vibrational modes while the short pulses allow the initial dynamics of this system to be studied in unprecedented detail revealing several new features whose origins are still under investigation.

For my family,
ad astra per aspera

Contents

List of Figures	iv
List of Tables	viii
Curriculum Vitae	x
1 Introduction	1
1.1 Photosynthetic Systems	1
1.1.1 Structure	1
1.1.2 Energy Transfer	4
1.2 Two-Dimensional Electronic Spectroscopy	5
1.3 Experiments	6
1.3.1 Excitonic Coherence	6
1.3.2 Electronic Structure of Carotenoids	8
1.4 Conclusions	8
2 Experimental Techniques	10
2.1 Introduction	10
2.2 NOPA	10
2.3 Compression	12
2.4 Pulse Characterization	17
2.5 Final Remarks	18
3 Evidence for wavelike energy transfer through quantum coherence in photosynthetic systems	19
3.1 Introduction	20
3.2 Methods	21
3.2.1 Sample Preparation	21
3.2.2 Data Acquisition	21
3.2.3 Data Modeling	21
3.3 Results	22
3.4 Discussion	25

3.5	Conclusions	28
4	Quantum Coherence Enabled Determination of the Energy Landscape in Light-Harvesting Complex II	29
4.1	Introduction	29
4.2	Methods	30
4.2.1	Sample Preparation	30
4.2.2	2D Electronic Spectroscopy	30
4.2.3	Simulations	31
4.3	Results and Discussion	33
4.4	Conclusions	38
5	Vibrationally-Mediated Dynamics in β-carotene Probed with Broad-band 2D Electronic Spectroscopy	40
5.1	Introduction	40
5.2	Methods	40
5.3	Results and Discussion	41
5.3.1	Long Time Dynamics	41
5.3.2	Short Time Dynamics	43
5.4	Conclusions	47

List of Figures

1.1	Crystal structures photosynthetic pigment-protein complexes that have exhibited excitonic coherence: (a) bacterial reaction center, ^{4,9} (b) FMO, ^{5,8} (c) LHCII, ^{6,10} (d) PE545. ^{7,11}	2
1.2	Molecular structures of common porphyrin-based photosynthetic pigments. The R group is a long hydrocarbon, phytol chain. λ_{Q_y} denotes the absorption maximum of the Q_y transition in diethyl ether. ¹³	3
1.3	Molecular structures of carotenoids.	3
1.4	<i>Left</i> Pulse geometry and timing used in 2D electronic spectroscopy experiments. <i>Right</i> Model 2D relaxation spectrum of a dimer system exhibiting a positive cross peak below the diagonal from population relaxation and a negative cross peak above the diagonal from excited state absorption.	6
1.5	Schematic of the adiabatic potential energy surfaces for the electronic states of a dimer in the presence of two phonon coordinates (q_1 and q_2) fluctuating with positive and negative correlation. ³²	8
1.6	Simplified three state energy level diagram describing a carotenoid molecule with the lifetimes given for β -carotene. The symmetries given in parentheses assume an idealized C_{2h} point group.	9
2.1	Schematic of the two-pass, visible NOPA. P1 and P2 compress the seed pulse prior to amplification. W is a pair of glass windows at Brewster's angle to stretch the pump pulse while P3 results in angular dispersion of the pump beam for increased overlap.	11
2.2	Example spectra produced by the NOPA in Fig. 2.1. The green spectrum was generated by a single pass in the NOPA and is centered at 550 nm with a FWHM of 70 nm. The red spectrum was generated using both passes through the NOPA crystal and is centered at 640 nm with a FWHM of 80 nm.	12
2.3	Picture of the SLM-based pulse compression apparatus.	14

2.4	(a) SLM display of a phase to be applied on a beam that is spectrally-dispersed horizontally. (b) SLM display of a vertical grating for diffraction optimized in the +1 direction. (c) SLM display for pulse compression in a diffraction-based configuration ($a+b$).	15
2.5	CCD image of spectrally-resolved beam after the SLM in reflective mode. (<i>top panel</i>) No phase applied across SLM (<i>bottom panel</i>) Applying phase across the SLM causes modulator replicas which appear as diffraction of frequencies at 0 to 2π transitions.	16
2.6	Experimental TG-FROG scans of the green NOPA spectrum in Fig. 2.2. (<i>top panel</i>) The pulse with no phase applied from the SLM displays long red and blue tails indicative of cubic phase. (<i>bottom panel</i>) The same pulse as above, but compressed to 12 fs with the SLM.	17
3.1	Selected two-dimensional electronic spectra of FMO are shown at waiting times from $T = 0$ to 600 fs demonstrating the emergence of the exciton 1-3 cross-peak (white arrows), amplitude oscillation of the exciton 1 diagonal peak (black arrows), the change in lowest-energy exciton peak shape and the oscillation of the 1-3 cross-peak amplitude. The data are shown with an arcsinh coloration to highlight smaller features: amplitude increases from blue to white (for a three-dimensional representation of the coloration see Fig. 3.4a).	23
3.2	(a) A representative two-dimensional electronic spectrum with a line across the main diagonal peak. The amplitude along this diagonal line is plotted as a function of waiting time in (b) with a black line covering the exciton 1 peak amplitude; the data are scaled by a smooth function effectively normalizing the data without affecting oscillations. A spline interpolation is used to connect the spectra; the times at which spectra were taken are denoted by tick marks along the time axis. (c) The amplitude of the peak corresponding to exciton 1 shown with a dotted Fourier interpolation. (d) The power spectrum of the Fourier interpolation in (c) is plotted with the theoretical spectrum showing beats between exciton 1 and excitons 2-7.	24
3.3	Beating Patterns Throughout the 2D Spectrum: A representative 2D spectrum ($T = 510$) is colored with an arcsinh scale to highlight the small cross-peak features. The black lines rising out of the spectrum show interpolations of the raw (unscaled) beating patterns at those locations from waiting times $T = 0$ to $T = 660$ fs. The power spectrum of each interpolation is shown in the corresponding graph with the expected exciton line spectra overlaid. For cross-peaks, the expected dominant beat frequency is shown in red.	25

3.4	The anticorrelation shown in the inset plot between the amplitude of the diagonal exciton peak (black line) and the ratio of the diagonal to anti-diagonal widths of the peak (red lines) is a characteristic predicted from theory for exciton quantum beating. ²⁵ This pattern would not arise from phonon coupling and highlights the change in integrated line strength associated with quantum beating.	26
3.5	(a) The raw amplitude of the exciton 1-3 cross-peak, with a Fourier interpolation of the points (dotted line). (b) The power spectrum of this interpolation (dotted line), the exciton beating line spectra of both excitons 1 and 3 (black), and the 1-3 beat frequency (red). We expect that the other frequencies may couple to this cross-peak but that the dominant frequency corresponds to the red transition. The apparent low-frequency peak is due to the growth of the cross-peak amplitude and appears as a peak because the data were demeaned (mean subtracted from the data) before the transform to improve numerical accuracy, pinning the zero frequency component to zero.	27
4.1	(a) Chlorophyll arrangement in LHCII trimer with Chl <i>a</i> and Chl <i>b</i> shown in green and blue, respectively. ⁸⁴ (b) Linear absorption spectrum of LHCII trimers at 77 K. Red sticks indicate the exciton energies determined in this experiment while black sticks are previously predicted values. ⁷⁵	32
4.2	(a) The real part of a representative 2D relaxation spectrum for $T = 250$ fs. (b) The real part of the nonrephasing 2D spectrum for $T = 250$ fs. (c) The amplitude of the diagonal cut of the nonrephasing 2D spectra as a function of waiting time. For the purposes of presentation, a cubic spline interpolation connects the data points that were acquired in 10 fs increments. For (a)-(c), amplitude increases from purple (negative) to white (positive).	33
4.3	The real parts of selected 2D nonrephasing spectra of LHCII are shown for waiting times between $T = 0$ fs and $T = 500$ fs to illustrate quantum beating of the diagonal features. The high energy Chl <i>a</i> peak (white arrows) can be seen in different stages of oscillations throughout the duration of the experiment. All spectra are shown normalized to their maximum value.	34
4.4	Power spectra of quantum beating in LHCII constructed from experimental 2D data (a) and theoretical simulations from the new model (b) and the model in ref. 75 (c) as described in the text. The beat frequency axis begins at 50 cm^{-1} to remove the strong DC component and contours are placed at 5% intervals. The boxes indicate the regions examined in detail in Fig. 4.5.	35

4.5	The boxed Chla regions of the power spectra in Fig. 4.4. The circled peak and arrow highlight features discussed in the text.	36
5.1	Representative real 2D (a) relaxation, (b) rephasing, and (c) non-rephasing spectra for β -carotene in 2-mTHF at long times ($T=325$ fs). The feature in the boxed region exhibits a lineshape characteristic of coupling to a high energy vibrational mode. The black arrow points to a cross peak near the diagonal that arises from the nonrephasing signal. Amplitude increases from purple (negative) through blue (zero) to white (positive).	42
5.2	Cuts of the real 2D rephasing spectra for $\lambda_t=555$ nm showing the oscillating phase of the lineshape of the transition in the boxed region in Fig. 5.1.	42
5.3	Representative spectra of the short time dynamics observed for (left) relaxation, (middle) rephasing, and (right) nonrephasing signals from β -carotene in 2-mTHF. The white and black arrows highlight non-rephasing features discussed in the text while the dynamics in the boxed region are presented in Fig. 5.4.	44
5.4	Integrated regions of 2D spectra indicated by the box in Fig. 5.3 showing clear beating in the amplitude of the rephasing cross peak.	45
5.5	Representative imaginary, nonrephasing 2D spectra. The white and black arrows are in the same location as those in Fig. 5.3 and highlight the irreversible change in lineshape observed for both features.	46

List of Tables

2.1	Sign of dispersion from common optical components	13
4.1	Exciton energies determined from the 2D electronic spectroscopy experiment compared with those calculated from previous models . . .	37

Acknowledgments

It has been impossible to compile this body of work without fully appreciating all who were involved in making this thesis possible. I first would like to thank my advisor, Graham R. Fleming. Graham provided me with countless opportunities over the years and capitalized on my need for deadlines but was always patient when it mattered.

To all of my fellow Flemingites old and new; there isn't one person who I didn't bother with questions over the years which always resulted in enlightening discussions. I would especially like to thank Greg Engel who took me under his wing from the beginning and mentored me throughout my entire graduate career. Also to the rest of the "room 2 crew" including Donatas Zigmantas, Elizabeth Read, Tae-Kyu Ahn, Gabriela Schlau-Cohen, Naomi Ginsberg, and Matt Graham, and the brilliant and patient theorists, Tomáš Mančal, Yuan-Chung Cheng, and Akihito Ishizaki, I was so lucky to work with. Jahan Dawlaty and Doran Bennett were extremely helpful in all things SLM related. I would also like to thank Nancy and Tiff, the true jack-of-all-trades, who made it possible to just focus on the science.

All of the work presented here was only possible through numerous collaborations. Bob Blankenship, Roberto Bassi, and Matteo Ballottari not only provided sample, but visited the lab contributing valuable insight with their expertise. Jeff Davis spent months visiting from Australia to help tackle β -carotene with 2D; a struggle that still continues now via Skype. I would also like to thank Jake Petrich who started me on the path of physical chemistry and informed me that I was absolutely going to apply to Berkeley as he had already told Graham of my "disrespect of authority" (I hope I lived up to this glowing recommendation).

Outside of the lab, my family's endless support carried me from day to day. Somehow between classes, teaching, qualifying exams, and experiments, or maybe because of them, I was also lucky enough to find the love of my life during graduate school. Benjamin Doughty was, and still is, my anchor. I do not know how I would've made it through this without him beside me. Last but certainly not least, I would like to thank George Holinga, a great listener and friend, and Greg Dalligner, my original homework buddy and usher extraordinaire.

DEPARTMENT OF CHEMISTRY, UNIVERSITY OF CALIFORNIA, BERKELEY
B77 HILDEBRAND HALL, BERKELEY, CA 94720
510.421.0060 • TCALHOUN@BERKELEY.EDU

TESSA R. CALHOUN

RESEARCH INTERESTS

- Structure-function relationships in natural systems
- Optics and development of advanced spectroscopic techniques
- Ultrafast phenomena

EDUCATION

- Ph. D.** Physical Chemistry, *University of California, Berkeley*, December 2010
B. S. Chemistry (with distinction), *Iowa State University*, May 2005

RESEARCH EXPERIENCE

University of California, Department of Chemistry, Berkeley, CA
Lawrence Berkeley National Laboratory, Physical Biosciences Division

Advisor: Graham R. Fleming

6/2005–12/2010:

Investigation of photosynthetic systems with two-dimensional electronic spectroscopy:

- Discovered quantum excitonic coherence in Fenna-Matthews-Olsen pigment protein complex
- Determined electronic structure of Light Harvesting Complex II through the study of quantum excitonic coherence
- Construction of SLM-based pulse shaper
- Studied electronic structure and nonadiabatic dynamics in the carotenoid, β -carotene

Iowa State University, Department of Chemistry, Ames, IA

Advisor: Jacob W. Petrich

3/2003–5/2005:

- Investigation of solvation dynamics of room-temperature ionic liquids with absorption, fluorescence, and time-correlated single-photon counting spectroscopies

Ames Laboratory, Ames, IA

Center for Sustainable Environmental Technologies

Advisor: Maohong Fan

8/2002–3/2003:

- Synthesis of ferric(VI)sulfate complex for water purification
1/2002–5/2002:
- Analysis of polymers created from coal fly ash via various titration techniques

North Dakota State University, Department of Chemistry, Fargo, ND

Advisor: Seth C. Rasmussen

6/2002–8/2002:

National Science Foundation Research Experience for Undergraduates Program

- Attempted synthesis of the conjugated polymer 2,3-Dimethylpyrrolo[3,4-*b*]pyrazine

6/2000–3/2001:

- Synthesis, purification, and characterization of 2,3-Didodecyl- and 2,3-Didecylthieno[3,4-*b*]pyrazines for conjugated polymer development

PUBLICATIONS

T. R. Calhoun and G. R. Fleming. “Quantum coherence in photosynthetic complexes”. *Phys. Stat. Sol. b* (**in press**).

G. S. Schlau-Cohen, T. R. Calhoun, N. S. Ginsberg, M. Ballottari, R. Bassi, and G. R. Fleming. “Spectroscopic elucidation of uncoupled transition energies in the major photosynthetic light-harvesting complex, LHCII,” *Proc. Natl. Acad. Sci. USA* **2010**, *107*, 13276–13281.

A. Ishizaki, T. R. Calhoun, G. S. Schlau-Cohen, and G. R. Fleming. “Quantum coherence and its interplay with protein dynamics in photosynthetic electronic energy transfer,” *Phys. Chem. Chem. Phys.* **2010 (cover article)**, *12*, 7319–7337.

T. R. Calhoun, N. S. Ginsberg, G. S. Schlau-Cohen, Y.-C. Cheng, M. Ballottari, R. Bassi, and G. R. Fleming. “Quantum coherence enabled determined of the energy landscape in Light Harvesting Complex II,” *J. Phys. Chem. B* **2009 (cover article)**, *113*, 16291–16295.

G. S. Schlau-Cohen, T. R. Calhoun, N. S. Ginsberg, E. L. Read, M. Ballottari, R. Bassi, and G. R. Fleming. “Mapping pathways of energy flow in LHCII with two-dimensional electronic spectroscopy,” *J. Phys. Chem. B* **2009**, *113*, 15352–15363.

T. Mančal, L. Valkunas, E. L. Read, G. S. Engel, T. R. Calhoun, and G. R. Fleming. “Electronic coherence transfer in photosynthetic complexes and its signature in optical spectroscopy,” *Spectroscopy—An International Journal* **2008**, *22*, 199–211.

E. L. Read, G. S. Engel, T. R. Calhoun, T. Mančal, T. K. Ahn, R. E. Blankenship, and G. R. Fleming. “Cross-peak specific two-dimensional electronic spectroscopy,” *Proc. Natl. Acad. Sci. USA* **2007**, *104*, 14203–14208.

G. S. Engel, T. R. Calhoun, E. L. Read, T. K. Ahn, T. Mančal, Y.-C. Cheng, R. E. Blankenship, and G. R. Fleming. “Evidence for wavelike energy transfer through quantum coherence in photosynthetic systems,” *Nature* **2007**, *446*, 782–786.

P. K. Chowdhury, M. Halder, L. Sanders, T. Calhoun, J. L. Anderson, D. W. Armstrong, X. Song, and J. W. Petrich. “Dynamic solvation in room-temperature ionic liquids,” *J. Phys. Chem. B* **2004**, *108*, 10245–10255.

D. D. Kenning, K. A. Mitchell, T. R. Calhoun, M. R. Funfar, D. J. Sattler, and S. C. Rasmussen. “Thieno[3,4-*b*]pyrazines: synthesis, structure, and reactivity,” *J. Org. Chem.* **2002**, *67*, 9073–9076.

PRESENTATIONS

Invited Speaker: “Quantum Coherence in Photosynthetic Complexes,” International Workshop on Nonlinear Optics and Excitation Kinetics in Semiconductors, Paderborn, Germany, August 2010.

Oral Presentation: “Vibrationally-Mediated Dynamics in β -Carotene Probed with Broadband 2D Electronic Spectroscopy,” XVII International Conference on Ultrafast Phenomena, Snowmass, CO, July 2010.

Invited Speaker: “Excitonic Coherence in LHCII,” Federation of Analytical Chemistry and Spectroscopy Societies Conference, Louisville, KY, October 2009.

Invited Speaker: “Excitonic Coherence in LHCII,” American Physical Society March Meeting, Pittsburgh, PA, March 2009.

Oral Presentation: “Observation of Quantum Coherence in Light Harvesting Complex II by Two-Dimensional Electronic Spectroscopy,” XVI International Conference on Ultrafast Phenomena, Stresa, Italy, June 2008.

Poster Presentation: “Dynamic Solvation in Room Temperature Ionic Liquids,” 229th American Chemical Society National Meeting, San Diego, CA, March 2005.

PROCEEDINGS

G. S. Schlau-Cohen, T. R. Calhoun, N. S. Ginsberg, M. Ballottari, R. Bassi and G. R. Fleming. “Elucidation of electronic structure and quantum coherence in LHCII with polarized 2D spectroscopy,” in *Ultrafast Phenomena XVII: Proceedings of the 17th International Conference*; Springer Series in Chemical Physics, **accepted**.

T. R. Calhoun, J. A. Davis, M. W. Graham, and G. R. Fleming. “Vibrationally-mediated dynamics in β -carotene probed with broadband 2D electronic spectroscopy,” in *Ultrafast Phenomena XVII: Proceedings of the 17th International Conference*; Springer Series in Chemical Physics, **accepted**.

M. W. Graham, T. R. Calhoun, A. Green, M. C. Hersam, and G. R. Fleming. “Two-dimensional electronic spectroscopy of semiconducting single-walled carbon nanotubes,” in *Ultrafast Phenomena XVII: Proceedings of the 17th International Conference*; Springer Series in Chemical Physics, **accepted**.

T. R. Calhoun, N. S. Ginsberg, G. S. Schlau-Cohen, Y.-C. Cheng, M. Ballottari, R. Bassi, and G. R. Fleming. “Observation of quantum coherence in Light-Harvesting Complex II by two-dimensional electronic spectroscopy,” in *Ultrafast Phenomena XVI: Proceedings of the 16th International Conference* (eds. P. Corkum, S. De Silvestri, K. A. Nelson, E. Riedle, and R. W. Schoenlein); Springer: Berlin, **2009**, 406–408.

G. S. Schlau-Cohen, T. R. Calhoun, G. S. Engel, E. L. Read, N. S. Ginsberg, D. Zigmantas, R. Bassi, and G. R. Fleming. “Mapping parallel pathways of energy flow in LHCII with broadband 2D electronic spectroscopy,” in *Ultrafast Phenomena XVI: Proceedings of the 16th International Conference* (eds. P. Corkum, S. De Silvestri, K. A. Nelson, E. Riedle, and R. W. Schoenlein); Springer: Berlin, **2009**, 598–600.

G. S. Engel, E. L. Read, T. R. Calhoun, T. K. Ahn, T. Mančal, R. E. Blankenship, and G. R. Fleming. “Two dimensional Fourier transform electronic spectroscopy: evolution of cross peaks in the Fenna-Matthews-Olson complex,” in *Ultrafast Phenomena XV: Proceedings of the 15th International Conference* (eds. P. Corkum, D. Jonas, K. J. D. Miller, and A. M. Weiner); Springer: Berlin, **2007**, 392–394.

LABORATORY EXPERIENCE

- Optical Instrumentation: home-built Ti:Sapphire oscillator and regenerative amplifier laser systems, non-collinear optical parametric amplifier (NOPA), spatial light modulator (SLM)-based 4-*f* pulse shaper, 2D electronic spectroscopy
- Proficient in MATLAB and LabVIEW

- Contributed research ideas and aided in the preparation of several grant proposals including DOE, NSF, SISGR, and DARPA

HONORS

- 2004 Barry M. Goldwater Scholar
- Member of Phi Beta Kappa

TEACHING EXPERIENCE

Head Graduate Student Instructor, 9/2007–12/2007:

General Chemistry and Quantitative Analysis I, University of California, Berkeley

Instructor: Richard J. Saykally

Graduate Student Instructor, 1/2007–5/2007:

General Chemistry II, University of California, Berkeley

Instructor: Richard J. Saykally

Graduate Student Instructor, 9/2005–12/2005:

General Chemistry I, University of California, Berkeley

Instructor: Richard J. Saykally

Teaching Assistant, 9/2003–12/2003:

General Chemistry I for Chemistry Majors, Iowa State University

Instructor: Jacob W. Petrich

REFERENCES

Prof. Graham R. Fleming
Melvin Calvin Distinguished Professor of Chemistry
Vice Chancellor of Research, University of California, Berkeley
Lawrence Berkeley National Laboratory, Physical Biosciences Division
510.643.2735 • fleming@cchem.berkeley.edu

Prof. Richard J. Saykally
Professor of Chemistry
University of California, Berkeley
510.642.8269 • saykally@berkeley.edu

Prof. Jacob W. Petrich
Chair and Professor of Chemistry
Iowa State University
515.294.9422 • jwp@iastate.edu

Chapter 1

Introduction

The ability to harvest and utilize energy from the sun has been perfected by nature to sustain life for organisms ranging from towering redwood trees to microscopic bacteria. In all of these systems, success hinges on efficient energy transfer through highly engineered networks of pigment-protein complexes. These networks are extensive, requiring the transfer of excitation energy from antennae complexes, where light energy is absorbed, to reaction centers, where the excitation is converted into chemical energy. Such performance is not currently possible in artificial photosynthetic systems. A direct comparison can be made to the internal quantum efficiency in organic semiconductors¹ which is limited by relatively small exciton diffusion lengths of ~ 5 nm.² Natural photosynthesis, however, maintains nearly 100% quantum efficiency over length scales of ~ 20 -100 nm.³ As such, the energy landscapes in natural photosynthetic systems and mechanisms by which energy traverses through them is an active area of research.

1.1 Photosynthetic Systems

1.1.1 Structure

The structures of pigment-protein complexes revealed by X-ray crystallography has significantly enhanced our understanding of photosynthetic systems. While structures of reaction centers are generally similar between different organisms, those of light-harvesting antennae vary greatly. Figure 1.1 shows the structures for a variety of photosynthetic complexes including the reaction center for purple bacteria,⁴ the Fenna-Matthews Complex (FMO) from green sulfur bacteria,⁵ Light Harvesting Complex II (LHCII) from higher plants,⁶ and phycoerythrin 545 (PE545) from marine algae.⁷ With the exception of the bacterial reaction center in Fig. 1.1*a*, these seemingly different complexes all perform the same general function of absorbing and transferring energy. In addition, all of these complexes have experimentally exhibited

long-lived quantum coherence⁸⁻¹¹ as will be discussed in more detail for FMO and LHCII below and in Chapters 3 and 4, respectively.

Despite their many structural differences, all of the complexes in Fig. 1.1 contain a dense packing of chromophores held in a precise configuration by the surrounding protein. As opposed to the common synthetic approach of using different molecules for donor and acceptor, nature relies on small subsets of similar molecules (Figs. 1.2 and 1.3) and carefully tunes their electronic properties to perform a variety of different functions. This results in broad absorption bands, which are beneficial for maximizing light absorption, but also causes complex energy landscapes making analysis of these systems difficult. The array of electronic structures is achieved through the use of three key mechanisms:

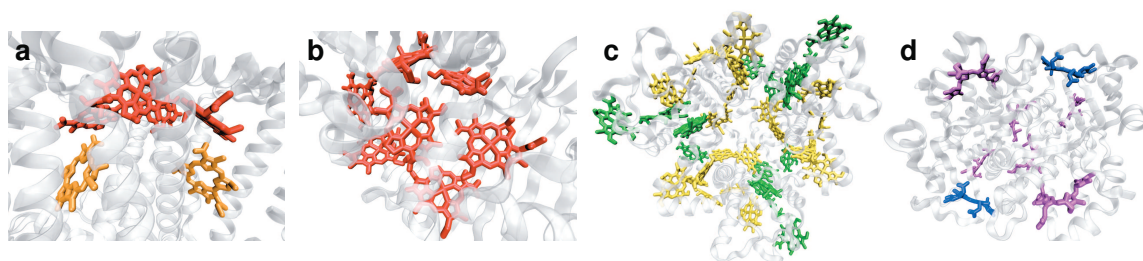


Figure 1.1: Crystal structures photosynthetic pigment-protein complexes that have exhibited excitonic coherence: (a) bacterial reaction center,^{4,9} (b) FMO,^{5,8} (c) LHCII,^{6,10} (d) PE545.^{7,11}

Chromophores. The first, and most obvious, method to manipulate the properties of a chromophore for a specific function is to change the molecule itself. Figure 1.2 gives the chemical structures for some of the chromophore molecules present in the complexes in Fig. 1.1. The majority of chromophores in all photosynthetic complexes are porphyrin-based and can be described by a “four orbital” model generating the two lowest energy singlet excitations aligned along orthogonal axes of the ring, Q_y and Q_x .¹² Focusing on the ground and HOMO-LUMO (Q_y) transition can reduce the description to a simple 2-level system. Slight alterations of the substituent groups on the main ring gives rise to the differences between bacteriochlorophyll (BChl), in which the Q_y excitation is in the near-IR, and chlorophyll (Chl) which absorbs in the visible.¹³ Smaller variations result in different types of (B)Chl (*ie.* Chl*a* and Chl*b*) shifting the electronic excitations by tens of nanometers.¹³ Removing the metal center from (bacterio)chlorophylls gives rise to (bacterio)pheophytins which are often found in reaction centers where they play a key role in electron transfer. Also shown is a bilin pigment which appears as an opened pheophytin ring but is often found in a linear conformation and is the only type of photosynthetic chromophore covalently

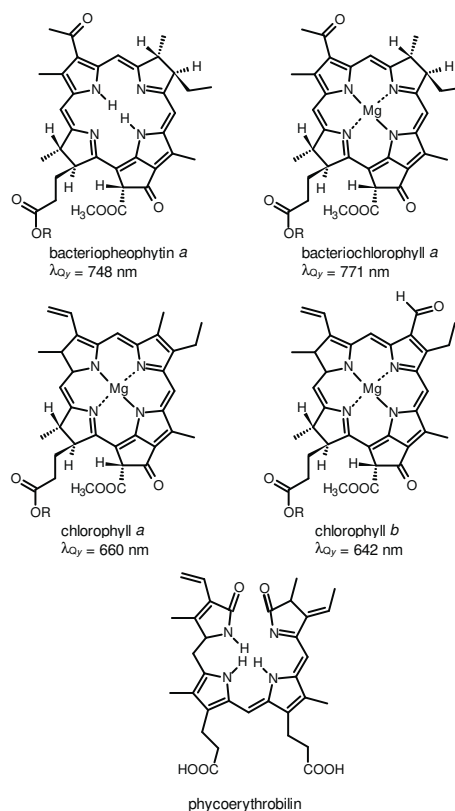


Figure 1.2: Molecular structures of common porphyrin-based photosynthetic pigments. The R group is a long hydrocarbon, phytol chain. λ_{Q_y} denotes the absorption maximum of the Q_y transition in diethyl ether.¹³

bound to the protein.¹² All of these molecules absorb and transfer energy in the initial steps of photosynthesis.

While porphyrin-based molecules are the most common light harvesting chromophores in nature, carotenoids are the second most common pigment class with functions ranging from light harvesting to photoprotection and structure. Figure 1.3 shows three different carotenoids that exist in photosynthetic complexes. Their elec-

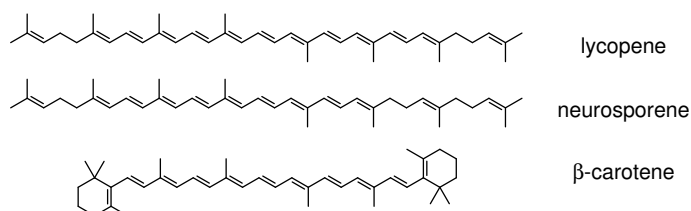


Figure 1.3: Molecular structures of carotenoids.

tronic properties are dominated by the long conjugated backbone and variations in its length result in the largest differences between carotenoids. For example, lycopene with a conjugation length, n , of 11 absorbs at 503 nm while neurosporene ($n = 9$) absorbs at 470 nm in the same solvent.¹⁴ The electronic structure of these chromophores will be discussed in more detail below.

Environment. From Fig. 1.1 it is clear that the chromophores are in close proximity to the surrounding protein. The protein matrix is an inhomogeneous environment in which each chromophore experiences unique pigment-protein interactions dependent on its specific position or “site”. Shifting of the chromophores’ electronic transitions to lower energies can arise through hydrogen bonding interactions or electrochromic effects from nearby amino acids.¹⁵ As an example, the FMO complex (Fig. 1.1*b*) contains 7 identical BChl molecules, but their site energies range from 790-820 nm due to different pigment-protein interactions.¹⁶

Electronic Coupling. The average distance between neighboring chromophore molecules in most photosynthetic complexes is ~ 10 Å.¹⁷ Here electrostatic interactions give rise to Coulombic coupling. As a result, excitations are delocalized and can be described by the Frenkel exciton model represented by the Hamiltonian

$$H_e = \sum_{n=1}^N \varepsilon_n |n\rangle \langle n| + \sum_{n < m} J_{nm} (|n\rangle \langle m| + |m\rangle \langle n|) \quad (1.1)$$

for N chromophores where ε_n are transition energies to the excited electronic states $|n\rangle$. In our discussion, ε_n is the Q_y transition of the chromophore in the n -th site of the protein, a so-called ‘site energy’. The excitonic coupling between the n -th and m -th chromophores in different sites of the protein is given by J_{nm} . The eigenvalues of Eq. 1.1 are the spectroscopically observable exciton energies. As the Coulombic coupling term, J , is dominated by the distance between molecules and the relative angles of their transition dipoles, it is apparent how the exact architecture of these structures gives rise to unique and complex electronic energy landscapes.

1.1.2 Energy Transfer

Historically, energy transfer has been described by the classical Förster theory.¹⁸ In this picture, after a donor is excited, the bath equilibrates quickly to localize the excitonic wavefunction on the donor. The excitation is subsequently transferred nonradiatively from the donor to an acceptor exciton. The fast bath equilibration destroys phase information leading to an irreversible, hopping motion of the energy. Förster theory, however, is limited to a regime in which the coupling between chromophores is weaker than their respective interactions with the bath.¹⁹ As already

alluded to in the previous section, this criterion is not always met in photosynthetic complexes.

Alternatively, we can examine the excitation's dynamic evolution with the time propagation of the density matrix:

$$\begin{aligned}
 |\Psi(t)\rangle\langle\Psi(t)| &= |a|^2 |e_1\rangle\langle e_1| + |b|^2 |e_2\rangle\langle e_2| \\
 &+ ab^* e^{-i(\omega_1-\omega_2)t} |e_1\rangle\langle e_2| \\
 &+ a^* b e^{i(\omega_1-\omega_2)t} |e_2\rangle\langle e_1|
 \end{aligned} \tag{1.2}$$

The first two terms are stationary and describe populations while the last two terms, which evolve with phase factors related to the energy difference between excitons, are quantum coherences. If energy transfer through the complex were to occur on the same timescale of these superpositions, it would behave quantum-mechanically instead of in the classical, hopping manner. This wavelike motion of energy is reversible, avoiding local minima, as the excitation searches for the energy sink to exit the complex. Recent theoretical calculations have also shown how this quantum coherence can promote unidirectional energy flow²⁰ and increase the overall efficiency of energy transfer when aided by noise from the protein environment.^{21,22}

1.2 Two-Dimensional Electronic Spectroscopy

Two-Dimensional (2D) Electronic Spectroscopy is sensitive to the phase evolution in Eq. 1.2 making it an ideal experimental tool to study energy transfer in photosynthetic systems. In addition, the ability to separate signals along a second dimension, here the excitation energy axis, provides information on the energy landscape of the system not accessible by other nonlinear spectroscopic techniques. Details of the theory²³ and experimental apparatus²⁴ have been described elsewhere. Briefly, an ultrafast laser source is split into three successive pulses which are focused onto the sample in a box geometry (Fig. 1.4 *left*). The resulting signal emerges in phase-matched direction collinear with a fourth, local oscillator pulse generating an interferogram as they are spectrally-resolved on a CCD camera. The first interaction with the sample creates a coherence between the ground and an excited state that is allowed to propagate for a time τ before the second pulse arrives. This second interaction can create a population or electronic coherence that evolves for a waiting time (T) as described by Eq. 1.2. The third pulse acts as the probe resulting in the generation of the signal field. If pulse 1 precedes pulse 2 ($+\tau$) in the box geometry shown in Fig. 1.4, the signal produced in the phase-matched direction collinear with the local oscillator will be a photon echo arising from “rephasing” pathways. For $-\tau$, when pulse 2 arrives at the sample before pulse 1, a “nonrephasing”, free-induction decay signal will be measured. At each T , τ is scanned producing a series of interferograms, and Fourier-transformation along the τ axis produces the final 2D relaxation spectrum (Fig. 1.4

right). The 2D spectrum can be thought of as a map that correlates absorption and emission events with excitation on the x -, ω_τ , axis and emission on the y -, ω_t , axis. Signals along the diagonal correspond to features in linear absorption spectra while off-diagonal features arise from electronic coupling, population transfer/relaxation, and excited state absorption. Electronic coherences during T generate features both on and off of the diagonal that oscillate in amplitude with a frequency equal to the energy difference between the excitons participating.^{25,26} Meanwhile, oscillations in the phase of the lineshape have theoretically been shown to indicate coupling to vibrational modes.^{27,28} This powerful technique is extended through the use of a tunable, broad bandwidth source providing ultrashort pulses as described in Chapter 2.

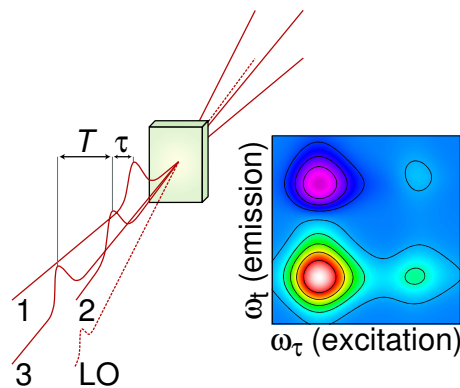


Figure 1.4: *Left* Pulse geometry and timing used in 2D electronic spectroscopy experiments. *Right* Model 2D relaxation spectrum of a dimer system exhibiting a positive cross peak below the diagonal from population relaxation and a negative cross peak above the diagonal from excited state absorption.

1.3 Experiments

1.3.1 Excitonic Coherence

FMO. Two-dimensional electronic spectroscopy was first used to investigate excitonic coherence in the Fenna-Matthews-Olson (FMO) complex as presented in Chapter 3. A component in green sulfur bacteria, FMO acts as an energetic wire connecting the chlorosome antenna complex to the reaction center. The structure of FMO in Fig. 1.1*b* shows 7 bacteriochlorophyll molecules held in each monomer of the trimer. While previous 2D experiments on FMO elucidated the energy transfer pathways,²⁹ a new 2D experiment was conducted to search for the beating signal arising from quantum coherences. Not only was signal consistent with excitonic coherence detected, it was observed to be surprisingly long-lived, lasting beyond the 660 fs duration of the experiment.⁸ This timescale is also longer than many of the exciton lifetimes in FMO

supporting the notion that energy transfer through the system is largely wavelike as opposed to hopping. While these initial experiments were conducted at 77 K, new work has revealed prolonged beating to 300 fs at 277 K.³⁰

LHCII. While the FMO experiment provided several exciting results, FMO itself is only present in a small subset of photosynthetic bacteria. Thus, the question remained as to whether the quantum mechanical motion of energy in photosynthetic complexes was a universal phenomenon. Given the structural differences apparent in Fig. 1.1, the ubiquitous presence of long-lived excitonic coherence would provide evidence of an underlying pattern essential to the design of these natural systems that gives rise to this phenomenon. Light Harvesting Complex II (LHCII) of higher plants contains >50% of all chlorophyll on Earth making it particularly well suited to answer this question. The structure of LHCII (Fig. 1.1c) is trimeric with each monomer containing 8 Chl*a* and 6 Chl*b* molecules. It is immediately obvious that this is a much more complex system than FMO and, therefore, presents several experimental challenges. First, the broad absorption in the visible afforded by the two distinct types of chromophores requires broadband excitation. In addition, the sheer number of chromophores generates a complex energy landscape and congested spectra. The same methodology applied to FMO in Chapter 3 would result in spectra of multiple overlapping features all beating with different frequencies making it impossible to extract information. Chapter 4 discusses the extension of 2D electronic spectroscopy to measure and isolate quantum coherence signals in LHCII. Not only is long-lived coherence again observed, but a coherence power spectrum is produced providing a direct measurement of the energy landscape.¹⁰

Protein Environment. Unlike most artificial systems, nature has housed its active media in an inhomogeneous and carefully designed environment. The results of initial experiments suggested the protein played an integral role in preserving the electronic coherence⁸ while theoretical modeling of long-lived coherence in the bacterial reaction center required strong correlation between fluctuations arising from the protein environment.⁹ Theoretical calculations have specifically implicated the role of the α -helices as a source of this correlation,³¹ and recent advancements in the theoretical framework used to treat electronic energy transfer in photosynthetic complexes have allowed the role of the protein environment to be explored in more depth.³² Figure 1.5 illustrates the effects of positively and negatively correlated fluctuations on the electronic states of a dimer system. In the case of positive correlation, the energy barrier between the states is reduced resulting in more delocalization, promoting coherence. For negative correlation, the opposite is true and coherence is prevented. As the determination of correlation as being positive or negative is based on the position and orientation of the molecules relative to common protein phonon modes to which they are coupled, the importance of the chromophores' organization within the

protein becomes apparent.

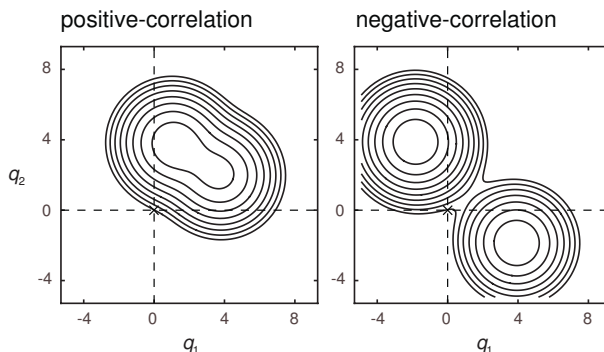


Figure 1.5: Schematic of the adiabatic potential energy surfaces for the electronic states of a dimer in the presence of two phonon coordinates (q_1 and q_2) fluctuating with positive and negative correlation.³²

1.3.2 Electronic Structure of Carotenoids

A full understanding of photosynthetic excitation energy transfer requires the consideration of the electronic structure and dynamics of carotenoids. The ability of carotenoids to perform opposing functions, contributing excitation energy as light harvesters and eliminating excess energy to aid in photoprotection, makes their energy landscape of particular interest. The electronic structure of carotenoids is often described with a simple picture as shown in Fig. 1.6. This three state model depicts a strong transition from the ground state (S_0) to the second excited singlet state (S_2) while direct excitation to S_1 is forbidden due to the C_{2h} -like symmetry of the conjugated backbone.¹⁴ This model, however, does not explain many of the experimental observations related to these molecules resulting in a vast body of work debating the true electronic structure of these seemingly simple pigments.^{14,33} Much of this work surrounds the hypothesized presence of dark states energetically intermediate to S_2 and S_1 (for a recent review see Ref. 34). The ultrafast relaxation to S_1 has made study the preceding dynamics particularly difficult. The combination of adaptive pulse shaping, as described in Chapter 2, with the information content from broadband 2D electronic spectroscopy provides a unique opportunity to investigate carotenoids. Chapter 5 will explore the dynamics of β -carotene in solution using this technique.

1.4 Conclusions

The results of 2D experiments on photosynthetic systems described in the following chapters reveal new insights into the design principles of nature. Extensions of

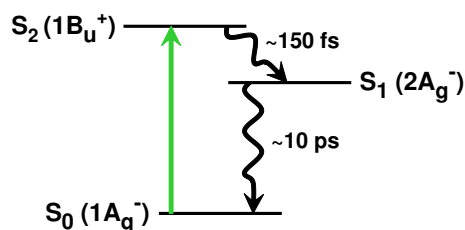


Figure 1.6: Simplified three state energy level diagram describing a carotenoid molecule with the lifetimes given for β -carotene. The symmetries given in parentheses assume an idealized C_{2h} point group.

2D spectroscopy to incorporate a broadband source and adaptive pulse shaping allow new systems to be studied in unprecedented detail. While the implications of the β -carotene experiments await further analysis, the existence of long-lived excitonic coherence in a wide range of photosynthetic complexes from bacteria to plants may explain the efficiency of energy transfer in these natural systems. Current experiments and theory imply that this phenomenon arises not only from the chromophores themselves, but from an active protein environment. A full understanding of the role of quantum mechanical energy transfer in natural photosynthesis could provide insight into fields ranging from alternative energy to quantum information.

Chapter 2

Experimental Techniques

2.1 Introduction

Photosynthetic systems have evolved to utilize the entire visible spectrum from 400-700 nm.¹² As introduced in the previous chapter, two-dimensional spectroscopy has proven itself as a useful technique to study complex energetics, but the extension of 2D spectroscopy to encompass the spectrally disparate resonances present in photosynthetic complexes requires an ultrabroad bandwidth source. To implement such a source, three major considerations must be addressed: generation, compression, and characterization of a broadband laser spectrum.

2.2 NOPA

Previous 2D electronic experiments had been limited to the wavelength range afforded by a Titanium:sapphire laser. This range can be extended through the phenomenon of optical parametric generation (OPG) in which a high intensity beam incident on a suitable nonlinear crystal can be split into two lower frequency components satisfying energy conservation:

$$\hbar\omega_p = \hbar\omega_s + \hbar\omega_i$$

where ω_p is the frequency of the incident pump beam, and ω_s and ω_i represent the resulting signal and idler beams, respectively, with the condition $\omega_i < \omega_s < \omega_p$.³⁵ Similarly momentum must be conserved with the phase matching condition:

$$\hbar\mathbf{k}_p = \hbar\mathbf{k}_s + \hbar\mathbf{k}_i$$

with \mathbf{k}_p , \mathbf{k}_s , and \mathbf{k}_i representing the wave vectors of the pump, signal, and idler beams, respectively. As OPG is a spontaneous process, a seed beam is often introduced coincident with the pump beam on the nonlinear crystal to amplify the desired spectral

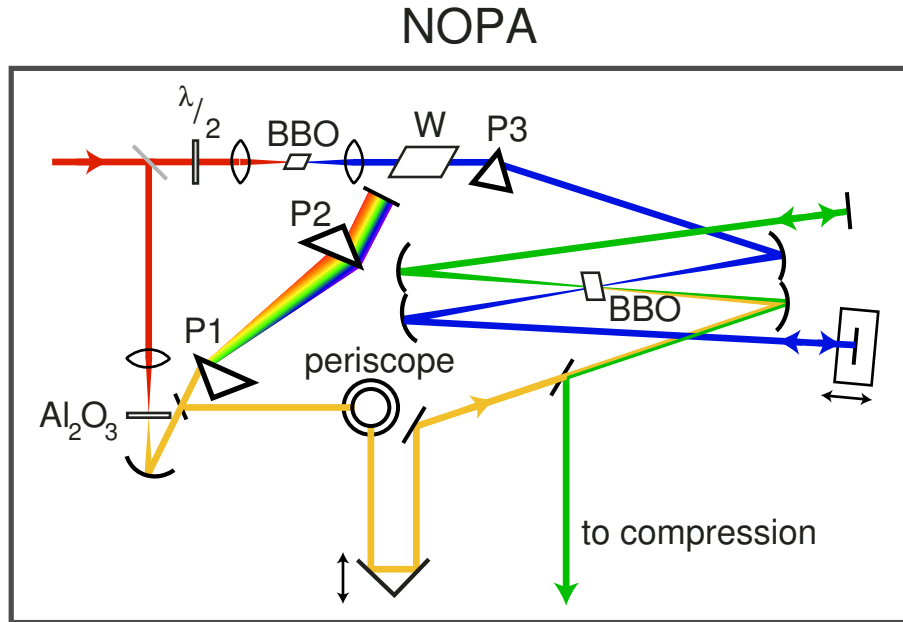


Figure 2.1: Schematic of the two-pass, visible NOPA. P1 and P2 compress the seed pulse prior to amplification. W is a pair of glass windows at Brewster's angle to stretch the pump pulse while P3 results in angular dispersion of the pump beam for increased overlap.

region. If there is a nonzero angle between the pump and seed beams incident on the crystal, the phase-matching condition can be extended to achieved broadband signal in a so-called noncollinear optical parametric amplifier (NOPA).³⁵

Our home-built, visible NOPA allows for up to two passes through the NOPA crystal for dual-stage amplification as shown in Fig. 2.1. It is based on the design of Baltuška *et al.*³⁶ and is an update to a previously constructed NOPA.³⁷ The new NOPA incorporates several features to increase the bandwidth including a prism pair to compress the seed beam, a pair of windows to stretch the pump beam, and a prism to tilt the phase front of the pump increasing the effective phase-matching bandwidth.^{36,38} Examples of spectra produced by the NOPA are shown in Fig. 2.2 and were used in the experiments that will be discussed in Chapters 4 and 5 for the red and green traces, respectively.

The largest drawback of our apparatus is the spatial mode quality of the resulting visible beam. It is important to realize that the original design of Baltuška *et al.* was pumped with a 1 kHz repetition rate commercial amplifier producing 150 μJ pulses while our 3.4 kHz home-built amplifier generates pulses of only 35 μJ . As shown by Piel *et al.* large differences in pump energy can dramatically affect the focal properties of the NOPA.³⁹ Future optimizations of the NOPA may benefit from including aspects of the Piel design³⁹ as well as splitting the pump pulse for the two stages of amplification

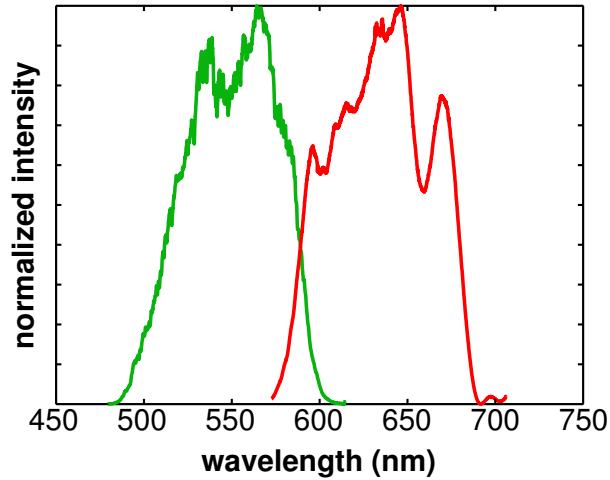


Figure 2.2: Example spectra produced by the NOPA in Fig. 2.1. The green spectrum was generated by a single pass in the NOPA and is centered at 550 nm with a FWHM of 70 nm. The red spectrum was generated using both passes through the NOPA crystal and is centered at 640 nm with a FWHM of 80 nm.

so that the effects to the spatial mode of the pump caused by the first pass are not amplified by the second pass. To mitigate the imperfections of the spatial mode in the current setup, a cylindrical mirror telescope was built after the SLM.

2.3 Compression

One key advantage of using a broadband laser spectrum is the increased time resolution afforded by short pulses. Optimal compression of the NOPA spectrum is required to produce the shortest pulses. To determine the best compression scheme it is beneficial to first consider the source of dispersion effects that lengthen the pulse. The phase of the electric field, $\phi(\omega)$, can be expanded about the central frequency, ω_0 , as

$$\begin{aligned} \phi(\omega) = & \phi(\omega_0) + \left(\frac{d\phi}{d\omega}\right)_{\omega_0} (\omega - \omega_0) + \frac{1}{2} \left(\frac{d^2\phi}{d\omega^2}\right)_{\omega_0} (\omega - \omega_0)^2 \\ & + \frac{1}{6} \left(\frac{d^3\phi}{d\omega^3}\right)_{\omega_0} (\omega - \omega_0)^3 + \frac{1}{24} \left(\frac{d^4\phi}{d\omega^4}\right)_{\omega_0} (\omega - \omega_0)^4 + \dots \end{aligned} \quad (2.1)$$

Where $\left(\frac{d\phi}{d\omega}\right)_{\omega_0}$ is the group delay (GD), $\left(\frac{d^2\phi}{d\omega^2}\right)_{\omega_0}$ is the group delay dispersion (GDD) or group velocity dispersion (GVD), also known as linear chirp, and $\left(\frac{d^3\phi}{d\omega^3}\right)_{\omega_0}$ is the third order dispersion (TOD), or cubic spectral phase. Positive linear chirp (+GVD)

	GVD	TOD
material	+	+
prism pair	-	-
grating pair	-	+

Table 2.1: Sign of dispersion from common optical components

can result from propagation through material and lengthens the pulse with red components arriving first as a function of time while for +TOD red and blue components arrive before the intermediate spectral region. In general, optical components affect the dispersion as shown in Table 2.1.

Given that significant sources of chirp in NOPA arise from material dispersion, a prism pair appears suitable for compression of the NOPA signal. Although a prism compression line was initially constructed for the NOPA, it is well known that this geometry overcompensates TOD.⁴⁰ This results in significant residual cubic phase from the prism pairs in the compression and precompression lines. Optimal compression of the NOPA therefore requires a second compression stage. From Table 2.1 the obvious solution to eliminate the residual cubic phase may be the introduction of a pair of gratings. There are, however, many drawbacks to this arrangement. Gratings have only a maximum compressor efficiency of $\sim 70\%$ over limited bandwidth, are not easily adaptable to changes in the output chirp of the NOPA that may arise from different alignments, and will not balance higher orders of chirp. Several examples of NOPA outputs being compressed to sub-10 fs through the use of chirped mirrors have been reported,^{41,42} but these configurations are also not easily adaptable limiting the tunability of the NOPA. A flexible pulse compression scheme can be realized through the use of a spatial light modulator (SLM).⁴³

Figure 2.3 shows our SLM adaptive pulse shaping apparatus built with a $4f$ geometry. The beam, input from the right, is first incident on a grating. To reduce the loss that is introduced by standard gratings, a transmissive volume phase holographic grating (600 l/mm, 600 nm, Wasatch Photonics) is used with an average diffraction efficiency of 80% over the entire spectral bandwidth independent of polarization. At a distance f from the grating, a focusing optic collimates the beam while simultaneously focusing the individual spectral components onto the SLM placed in the Fourier plane at another distance f from the optic. The phase of each color can then be controlled independently in the frequency domain by varying the refractive index of the separate SLM pixels. The beam is reflected back on itself to emerge from the pulse shaping line with minimal change in spatial properties.

The first consideration in design of the SLM compression line is to ensure the separation of spectral components, ie. avoiding space-time coupling effects.⁴⁴ The radius of the focal spot for each spectral component should be smaller than the pixel

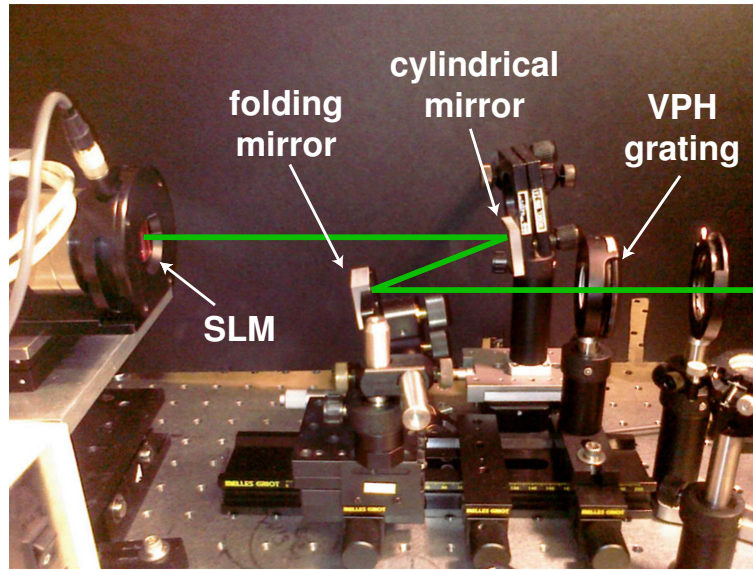


Figure 2.3: Picture of the SLM-based pulse compression apparatus.

size and can be calculated, assuming Littrow alignment of the grating, with:

$$w_0 = 4 \ln(2) \frac{f\lambda}{\pi w_{in}}$$

where w_{in} and w_0 are the FWHM of the spatial mode of the beam at the input and focal spot, respectively, and f is the focal length of the focusing optic. In our apparatus, a cylindrical mirror ($f = 19.07$ cm, CVI) is used to spread the beam over more vertical pixels reducing the possibility of damaging the SLM. The cylindrical mirror is also advantageous relative to a spherical optic as it allows the reflected beam to be offset vertically without introducing spherical aberration. When aligning the $4f$ line, it is common to encounter spatial chirp in the output beam. This can arise either from the SLM not being positioned in the focal plane of the cylindrical mirror or from an offset in the tilt of the horizontal axis of the grating or cylindrical mirror relative to each other.

We use a phase-only 2D SLM (PPM x8267, Hamamatsu) consisting of 768×768 optically-addressed pixels with a size of $25 \mu\text{m}$. For proper operation, two SLM calibrations are required. The SLM operates similarly to a computer monitor in which each pixel can be adjusted with a grayscale value from 0 to 256. It then first needs to be determined how much phase each grayscale value applies which is done by measuring the birefringence induced by the SLM. The polarizer on the front of the SLM is rotated 45° , and a crossed polarizer is placed at the output of the pulse shaping apparatus. The intensity of different wavelengths of the beam can be measured for

each grayscale value on the SLM and fit to a form:

$$I(g, \lambda) = \frac{I_0(\lambda)}{2} (1 + \cos\phi(g, \lambda))$$

where I is the measured intensity and the phase ϕ can be expanded as a polynomial in both the grayscale value, g , and the wavelength, λ . In our measurements, the first ~ 28 grayscale values were excluded from the fit as they scale nonlinearly with phase. This calibration only needs to be repeated for large changes in the spectrum of the pulse or if the drive voltage of the SLM is changed. The second calibration determines which wavelengths are incident on which pixels and must be repeated anytime the alignment of the NOPA or pulse shaping apparatus is adjusted. A single vertical column of pixels displays a pattern to diffract the frequencies incident on it in a different direction than the spectrum interacting with the rest of the SLM. By spectrally-resolving the output of the SLM line on a CCD camera, this column of pixels or “slit” results in a sharp dip in the amplitude of the laser spectrum for the wavelength components in the slit region. The slit is moved horizontally across the SLM with the resulting spectrum imaged such that SLM position of all wavelength components of the spectrum can be determined. As expected, the grating creates a linear distribution of wavelengths across the SLM.

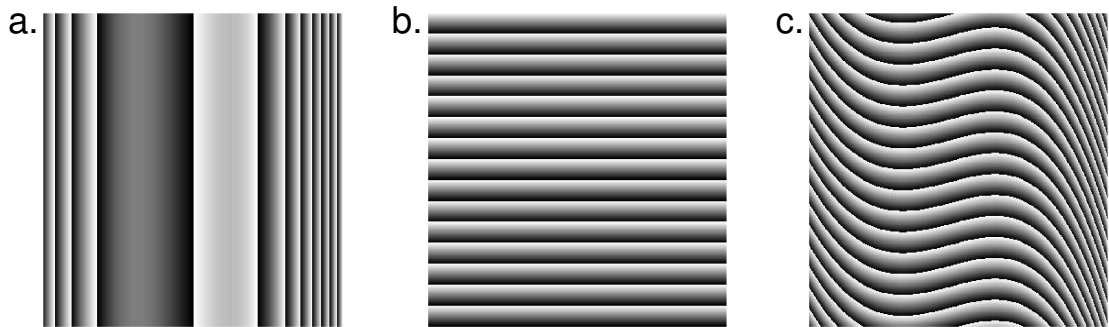


Figure 2.4: (a) SLM display of a phase to be applied on a beam that is spectrally-dispersed horizontally. (b) SLM display of a vertical grating for diffraction optimized in the +1 direction. (c) SLM display for pulse compression in a diffraction-based configuration ($a+b$).

As the amount of phase that can be applied by the SLM is limited, the modulus of the desired phase with respect to 2π is experimentally applied giving rise to an SLM display similar to that shown in Fig. 2.4a. In its initial implementation, the SLM was used only in reflective mode with this type of display resulting in artifacts in the spectrum as diffraction of wavelengths present at transitions between 0 and 2π phase on the SLM (Figure 2.5). Such artifacts had been observed previously through

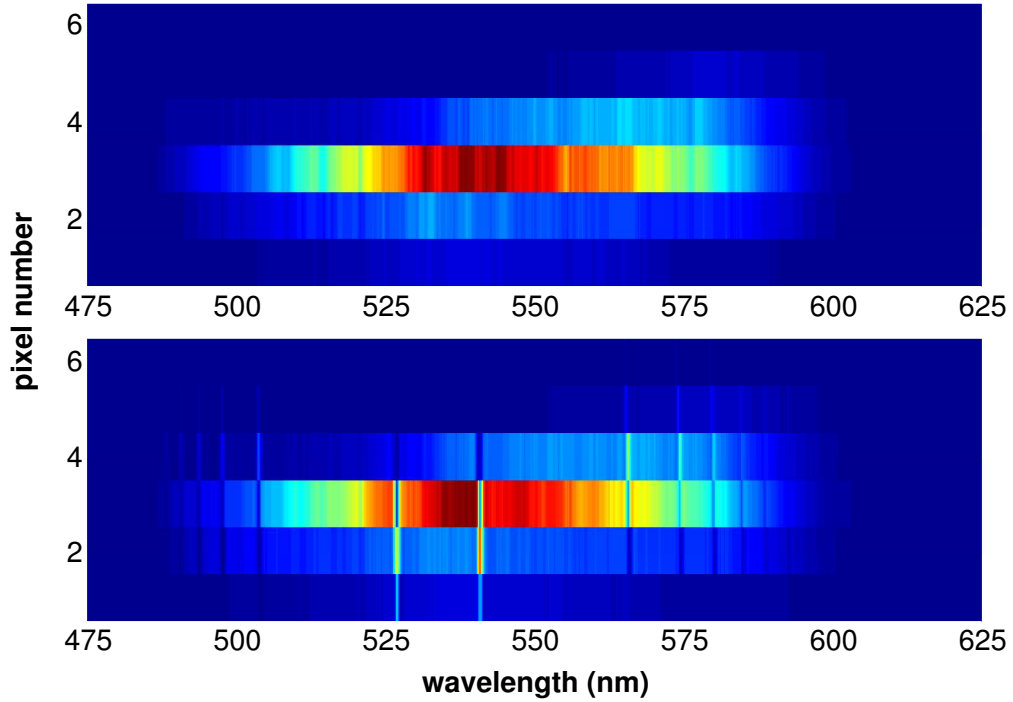


Figure 2.5: CCD image of spectrally-resolved beam after the SLM in reflective mode. (*top panel*) No phase applied across SLM (*bottom panel*) Applying phase across the SLM causes modulator replicas which appear as diffraction of frequencies at 0 to 2π transitions.

interferometry and in the temporal domain by Vaughan *et al.* and identified as modulator replicas.⁴⁵ To reduce the presence of these replica artifacts, they simultaneously applied a grating along the dimension of the SLM orthogonal to the dimension the desired phase was applied⁴⁶ (Fig. 2.4). By using the first order of the diffracted beam, only those wavelength components experiencing the desired phase are collected. The introduction of this diffraction-based operation into our SLM setup significantly reduced the diffraction artifacts apparent in Fig. 2.5. In future, amplitude modulation of the laser spectrum may also be possible with this diffraction-based alignment. Despite using an SLM that only allows for phase modulation, the amplitude of the diffracted beam can be shaped by making the grating applied to the SLM (Fig. 2.4b) more or less efficient for different colors through the adjustment of the phase range applied across each tooth of the grating.⁴⁶

2.4 Pulse Characterization

For previous experiments using the fundamental of the Ti:sapphire laser centered around 800 nm, the pulse timings were characterized by autocorrelation in a β -barium borate (BBO) crystal while the phase of the pulse was determined through second harmonic generation frequency-resolved optical gating (SHG-FROG).⁴⁷ Neither of these techniques, however, is suitable for characterization of the broadband NOPA output. For SHG, phase mismatch, dependent on the thickness of the BBO crystal, can result in the possible upconversion of only part of the spectral bandwidth. SHG-FROG is also not feasible due to the poor response of the CCD at the second harmonic frequencies of the NOPA wavelengths.

To overcome these issues, autocorrelation for pulse timing was achieved through two-photon absorption on a SiC photodiode (JEC 1, Electro Optical Components, Inc.)⁴⁸ The bandgap of SiC is 210-380 nm resulting in the absorption of only ultra-violet radiation leaving the visible fundamental of the NOPA undetected, and the two-photon absorption process is not limited by phase-matching conditions.

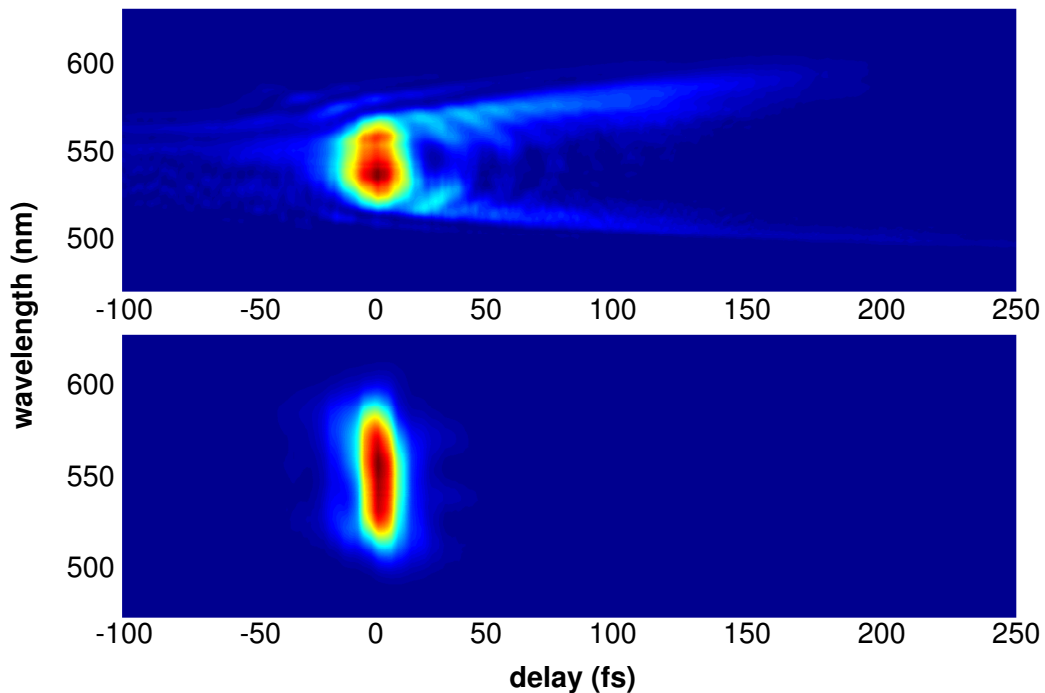


Figure 2.6: Experimental TG-FROG scans of the green NOPA spectrum in Fig. 2.2. (*top panel*) The pulse with no phase applied from the SLM displays long red and blue tails indicative of cubic phase. (*bottom panel*) The same pulse as above, but compressed to 12 fs with the SLM.

To determine the phase of the pulse, necessary for programming the SLM, transient grating (TG) FROG was conducted on a 2 mm thick fused silica substrate.⁴⁹ TG-FROG uses the beam geometry already present for the 2D experiments and has several advantages over SHG-FROG including a larger phase-matching bandwidth, the generation of signal at the same frequency as the input beam, and no ambiguity in the direction of time for the resulting phase.^{47,49}

Figure 2.6 shows two experimental TG-FROG traces for the laser spectrum given by the green trace in Fig. 2.2. In the top panel no phase is applied across the SLM and the pulse displays clear tails on the red and blue portions of the spectrum from the cubic phase introduced by the prism lines. The lower panel shows the compressed, 12 fs (FWHM) pulse produced after proper phase compensation by the SLM. Optimal compression was determined in an open feedback loop with the phase from the FROG algorithm fit to a series of polynomials as given by Eq. 2.1 before being applied to the SLM. The possibility of improved compression through a closed feedback loop to optimize the intensity of the SiC two-photon absorption was not explored and is left for future experiments.

2.5 Final Remarks

A few concerns are raised when the broadband pulses discussed in this chapter are incorporated into a 2D experimental apparatus. While broadband 2D setups have recently been designed,⁵⁰ the apparatus currently used does contain dispersive optics, specifically the diffractive optics and fused silica wedges used to generate the τ delay. No significant changes in the phase of the pulses were observed in our TG-FROG scans for the different wedge positions associated with the full range of our τ scans as has similarly been shown by others.⁵¹

Chapter 3

Evidence for wavelike energy transfer through quantum coherence in photosynthetic systems

Adapted with permission from *Nature*, **446**, 782-786 (2007). Copyright 2007 Nature Publishing Group.

Photosynthetic complexes are exquisitely tuned to capture solar light efficiently, and then transmit the excitation energy to reaction centers, where long term energy storage is initiated. The energy transfer mechanism is often described by semiclassical models that invoke ‘hopping’ of excited-state populations along discrete energy levels.^{12,15} Two-dimensional Fourier transform electronic spectroscopy^{23,24,52} has mapped²⁹ these energy levels and their coupling in the Fenna-Matthews-Olson (FMO) bacteriochlorophyll complex (Fig. 1.1*b*), which is found in green sulphur bacteria and acts as an energy ‘wire’ connecting a large peripheral light-harvesting antenna, the chlorosome, to the reaction center.^{5,53,54} The spectroscopic data clearly document the dependence of the dominant energy transport pathways on the spatial properties of the excited-state wavefunctions of the whole bacteriochlorophyll complex.^{29,55} But the intricate dynamics of quantum coherence, which has no classical analogue, was largely neglected in the analyses—even though electronic energy transfer involving oscillatory populations of donors and acceptors was first discussed more than 70 years ago,⁵⁶ and electronic quantum beats arising from quantum coherence in photosynthetic complexes have been predicted^{57,58} and indirectly observed.⁵⁹ Here we extend previous two-dimensional electronic spectroscopy investigations of the FMO bacteriochlorophyll complex, and obtain direct evidence for remarkably long-lived electronic quantum coherence playing an important role in energy transfer processes within this

system. The quantum coherence manifests itself in characteristic, directly observable quantum beating signals among the excitons within the *Chlorobium tepidum* FMO complex at 77 K. This wavelike characteristic of the energy transfer within the photosynthetic complex can explain its extreme efficiency, in that it allows the complexes to sample vast areas of phase space to find the most efficient path.

3.1 Introduction

In two-dimensional Fourier transform electronic spectroscopy, three pulses and a strongly attenuated local oscillator are incident on the sample. (For a detailed description of the method and the apparatus used in this study, see refs. 24, 52, 60) In the simplest time domain representation, the first pulse creates a coherence that evolves for time τ , then the second pulse creates an excited-state population that evolves for time T , and the third pulse creates a coherence that accumulates phase in the opposite direction for time t before rephasing occurs and a signal pulse is emitted in the unique phase-matched direction. The full electric field of the signal pulse is measured through heterodyne detection using spectral interferometry. In a frequency domain representation, two-dimensional Fourier transform electronic spectroscopy probes electronic couplings and energy transfer in molecules by mapping how excitations before the waiting time, T , affect emission after the waiting time. The coherence wavelength represents the initial excitation, while the rephasing wavelength can be thought of as the subsequent emission. Without coupling, contributions from excited-state absorption and emission cancel each other, yielding no off-diagonal peaks in the spectrum that signal such coupling. But in the presence of coupling, the cancellation is no longer complete and a so-called cross-peak emerges.⁶¹ Two-dimensional spectroscopy thus provides an excellent probe of the coupling between energy levels.

In the present experiment, we use two-dimensional electronic spectroscopy to observe oscillations caused by electronic coherence evolving during the waiting time in FMO. Such quantum coherence, a coherent superposition of electronic states analogous to a nuclear wavepacket in the vibrational regime, is formed when the system is initially excited by a short light pulse with a spectrum that spans multiple exciton transitions. Theoretical predictions indicate that both the amplitudes and shapes of peaks will contain beating signals with frequencies corresponding to the differences in energy between component exciton states.²⁵

3.2 Methods

3.2.1 Sample Preparation

The FMO sample was isolated from *Chlorobium tepidum* as published previously.⁵ The sample was dissolved in a buffer of 800 mM tris/HCl pH 8.0, 50 mM NaCl with 0.1% lauryldimethylamine oxide as a detergent. The sample was then mixed 65:35 v/v in glycerol and placed in a 200 μm quartz cell (Starna). The sample was cooled in a cryostat (Oxford Instruments) to 77 K. The absorbance of the sample at 805 nm was then measured to be 0.16.

3.2.2 Data Acquisition

A home-built oscillator was used to seed a home-built regenerative amplifier to produce a 3.4 kHz pulse train of 41 fs pulses centered about 808 nm with a spectral width of 31 nm FWHM.⁶² The stability of the laser system through the data acquisition period was measured to be 0.28% to 0.44%. The laser pulse width was measured with both autocorrelation (38 fs FWHM) and FROG (41 fs FWHM).

A diffractive optic was used to create two pairs of phase-locked beams, and all beams were incident on the same optics, aside from the one-degree fused silica wedges (Almaz Optics) used for delay stages. The delay stages were calibrated using spectral interferometry and have been shown to have attosecond stability and reproducibility.^{24,63} During data collection, the coherence time was stepped in 4 fs steps from -600 to 600 fs. Waiting times were sampled at 0, 10, 20, 30, 40, 50, 65, 80, 95, 110, 125, 140, 155, 170, 185, 200, 220, 240, 260, 280, 300, 330, 360, 390, 420, 450, 480, 510, 540, 570, 600, 630, and 660 fs. Additional points were taken at -1,000 fs to ensure that the signal observed was not an artifact. The sample was moved after every third data point, and some data points were repeated to ensure that the sample was not degrading during measurements.

The local oscillator was attenuated with a neutral density filter combination of absorbance 3.5 at 800 nm. The total power incident on the sample was 15 nJ (5 nJ/pulse) focused to a spot size less than 70 μm . The resulting signal and heterodyne beam were frequency-resolved with a spectrometer (Acton Research) and captured on a 1,340 x 5 pixel region of our charge-coupled device (CCD) array (Princeton Instruments). Scatter subtraction, Fourier windowing and transformation to frequency-frequency space was done as reported previously.^{24,60} Pump-probe data were taken for accurate phasing of the two dimensional spectra.

3.2.3 Data Modeling

To model the beat patterns in the data series, a non-uniform fast Fourier transform algorithm was used to search for Fourier power series that matched the data

and were consistent with the expected power spectrum. Because of the unequal spacing, a unique answer does not exist. The non-uniform fast Fourier transform power spectra were estimated using a modified 4th-Jackson kernel, and the results were then transformed back using a standard fast Fourier transform library (FFTW; www.fftw.org).^{64,65} To scale the data and eliminate spectral components from population dynamics, a smooth function with an exponential growth of the order of the pulse width and an exponential decay matched to the population dynamics in the main peak was used.

3.3 Results

To observe the quantum beats, two-dimensional spectra were taken at 33 waiting times T , ranging from 0 to 660 fs. Representative spectra are shown in Figure 3.1. In these spectra, the lowest-energy exciton gives rise to a diagonal peak near 825 nm that clearly oscillates: its amplitude grows, fades, and subsequently grows again. The peak's shape evolves with these oscillations, becoming more elongated when weaker and rounder when the signal amplitude intensifies. The associated cross-peak amplitude also appears to oscillate. Surprisingly, the quantum beating lasts for 660 fs. This observation contrasts with the general assumption that the coherences responsible for such oscillations are destroyed very rapidly, and that population relaxation proceeds with complete destruction of coherence¹⁵ (so that the transfer of electronic coherence between excitons during relaxation is usually ignored).^{15,66,67}

We note that this issue has been discussed theoretically, and that some theoretical models include coherence among both donors and acceptors;⁶⁸ however, coherence must be treated between all chromophores to ensure that the model will accurately reproduce the dynamics of the system.⁶⁹ In the case of FMO, theoretical models indicate that electronic coherence should dephase on the timescale of the initial population transfer, established by experiment to be less than 250 fs for all but excitons 1 and 3 (refs. 15, 70). The strong quantum beating that we observe to last for at least 660 fs clearly exceeds the model predictions. We believe that to account for this long-lived coherence and provide an accurate description of the system, the protein must have a more active role in a realistic bath model; that is, it must be allowed to interact with both donors and acceptors, to enable coherence transfer and possibly the generation of new coherences.

Our further investigation of these spectral oscillations focuses on the best-resolved spectral features in the two-dimensional electronic spectra, that is, the lowest exciton diagonal peak and associated cross-peak. In Fig. 3.2, we show the amplitude oscillations with time along the main diagonal of the spectrum. Because of the non-uniform spacing of the data points, converting the data to a unique power spectrum is not possible; instead, we map the data onto a Fourier subspace using a non-uniform fast Fourier transform algorithm.⁶⁴ The sampled amplitude variations of the lowest-energy

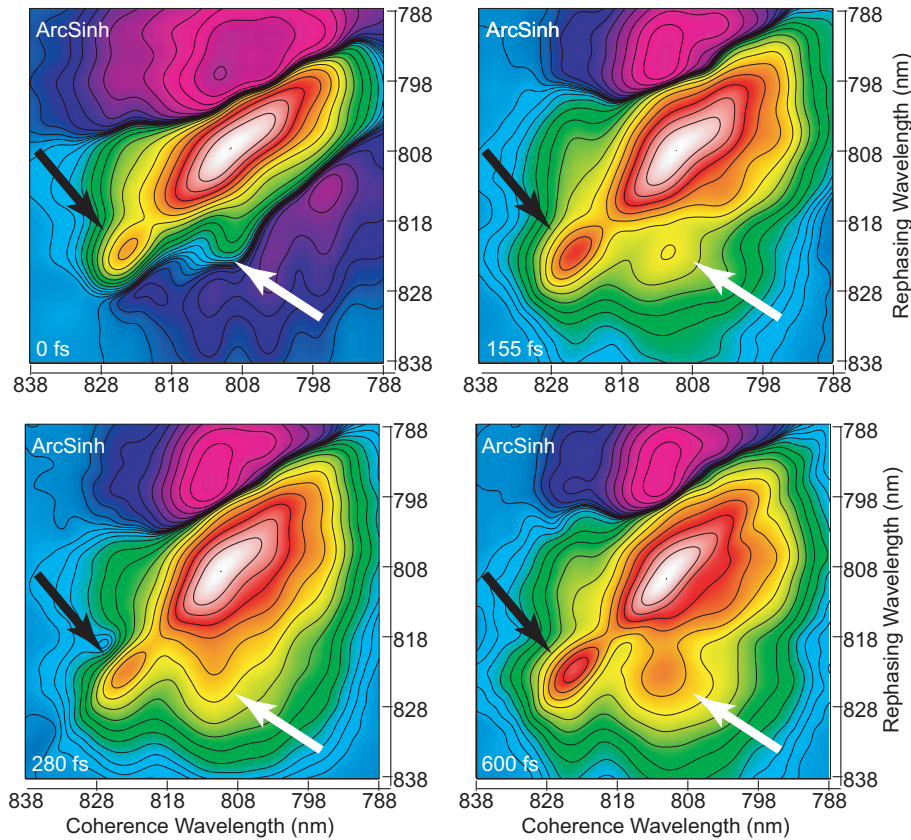


Figure 3.1: Selected two-dimensional electronic spectra of FMO are shown at waiting times from $T = 0$ to 600 fs demonstrating the emergence of the exciton 1-3 cross-peak (white arrows), amplitude oscillation of the exciton 1 diagonal peak (black arrows), the change in lowest-energy exciton peak shape and the oscillation of the 1-3 cross-peak amplitude. The data are shown with an arcsinh coloration to highlight smaller features: amplitude increases from blue to white (for a three-dimensional representation of the coloration see Fig. 3.4a).

exciton are shown with a Fourier interpolation from the subspace that was selected to be maximally consistent with the excitonic model. The theoretical excitonic coherence line spectrum was calculated using the exciton energies from the Hamiltonian in ref. 29, and the relative amplitudes were calculated using orientationally averaged response magnitudes for the associated cross-peak pathways.^{61,71,72}

The agreement between the data, the Fourier interpolation and the theoretical exciton spectrum demonstrates that the quantum beating observed is fully consistent with electronic coherence (analyses of beating in more peaks are shown in Fig. 3.3), and we present comparisons to an independent theoretical lineshape prediction to confirm this conclusion. Further, because the predicted orientational factor is identical for a diagonal exciton beating and for a cross-peak, that the amplitude of the

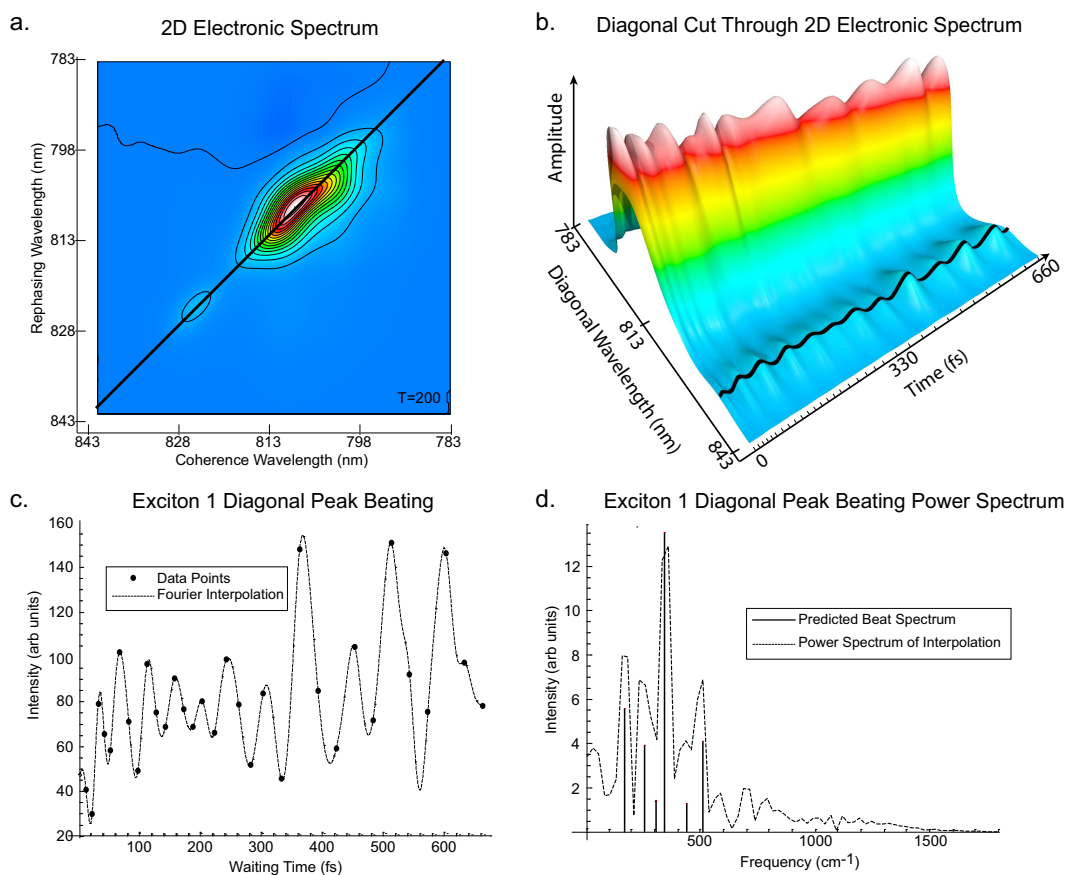


Figure 3.2: (a) A representative two-dimensional electronic spectrum with a line across the main diagonal peak. The amplitude along this diagonal line is plotted as a function of waiting time in (b) with a black line covering the exciton 1 peak amplitude; the data are scaled by a smooth function effectively normalizing the data without affecting oscillations. A spline interpolation is used to connect the spectra; the times at which spectra were taken are denoted by tick marks along the time axis. (c) The amplitude of the peak corresponding to exciton 1 shown with a dotted Fourier interpolation. (d) The power spectrum of the Fourier interpolation in (c) is plotted with the theoretical spectrum showing beats between exciton 1 and excitons 2-7.

beat is of the order of the amplitude of the cross-peak even at long times (>500 fs) indicates that the electronic coherence can play a significant role in determining the overall relaxation dynamics within the protein complex. This observation suggests that coherence relaxation pathways, including coherence transfer, should no longer be disregarded in theoretical models of photosynthetic protein complexes.

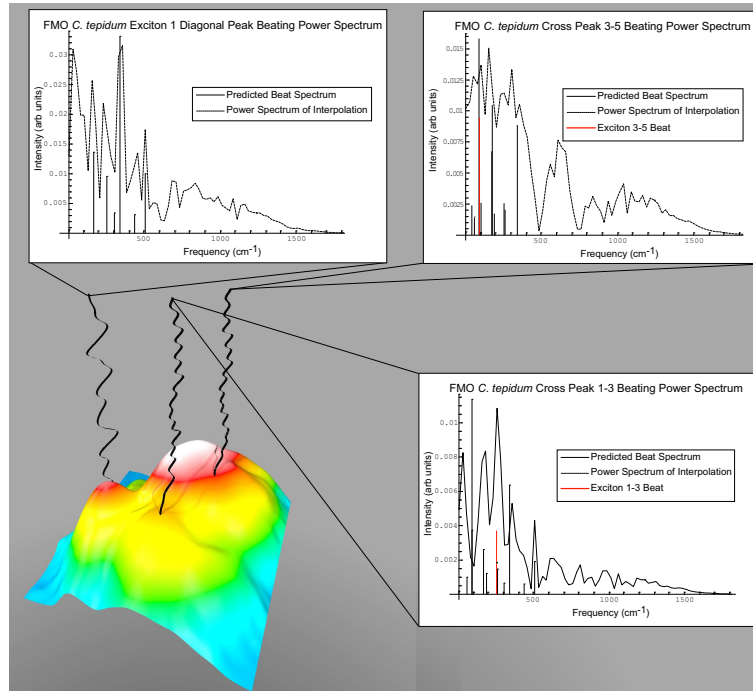


Figure 3.3: Beating Patterns Throughout the 2D Spectrum: A representative 2D spectrum ($T = 510$) is colored with an arcsinh scale to highlight the small cross-peak features. The black lines rising out of the spectrum show interpolations of the raw (unscaled) beating patterns at those locations from waiting times $T = 0$ to $T = 660$ fs. The power spectrum of each interpolation is shown in the corresponding graph with the expected exciton line spectra overlaid. For cross-peaks, the expected dominant beat frequency is shown in red.

3.4 Discussion

A predicted²⁵ signature of quantum beating in a dimer system is out-of-phase modulation of the diagonal and antidiagonal widths of a peak relative to its amplitude, with the peak predicted to become rounder as it gets stronger. Figure 3.4 documents precisely this behaviour in the lowest exciton state. We note that if this oscillation were due to vibrational wavepacket motion, the exciton peak would be expected instead to oscillate in frequency but maintain constant volume. The peak shape oscillations we see have not previously been observed in two-dimensional spectra, in which the peak width along the antidiagonal direction is generally an indicator of the extent of homogeneous broadening, whereas the peak width along the diagonal provides a measure of inhomogeneous broadening. In this context, the width modulation we observe would be akin to losing memory of the initial state, and subsequently regaining that memory. Clearly, this interpretation is not applicable while coherence persists. The unusual nature of the width modulation evident in our data

and its agreement with the predicted²⁵ characteristics of quantum beating further strengthens our conclusion that the beating we measure is due to excitonic quantum coherence.

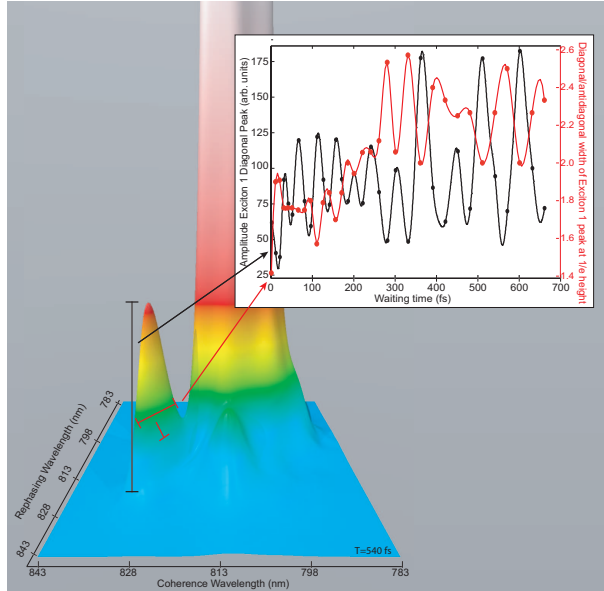


Figure 3.4: The anticorrelation shown in the inset plot between the amplitude of the diagonal exciton peak (black line) and the ratio of the diagonal to anti-diagonal widths of the peak (red lines) is a characteristic predicted from theory for exciton quantum beating.²⁵ This pattern would not arise from phonon coupling and highlights the change in integrated line strength associated with quantum beating.

Figure 3.5 shows that a Fourier interpolation of the beating spectrum apparent in the cross-peak between excitons 1 and 3 can again be explained by the expected exciton beating spectrum. The beating signal shows frequency components from all excitons coupled to either excitons 1 or 3, and a very strong component from the beat frequency between the two coupled excitons (1 and 3) that give rise to the cross peak. However, the cross-peak amplitude and associated beating do not appear strongly at time $T = 0$; this provides strong evidence for the existence of electronic coherence transfer in this system, with one superposition, for example between excitons 3 and 5, transferred into a superposition between excitons 3 and 1.

The observations illustrated in Figs. 3.2-3.5 clearly demonstrate that any full description of FMO dynamics needs to account for coherence between donors and acceptors, and for coherence transfer on a similar timescale to population relaxation. While our spectra are recorded at 77 K and the coherence among members of the ensemble will dephase faster at higher temperatures, quantum coherence will also be important at higher temperatures. This is because the underlying Hamiltonian, dynamics and relaxation pathways associated with superposition states of individual

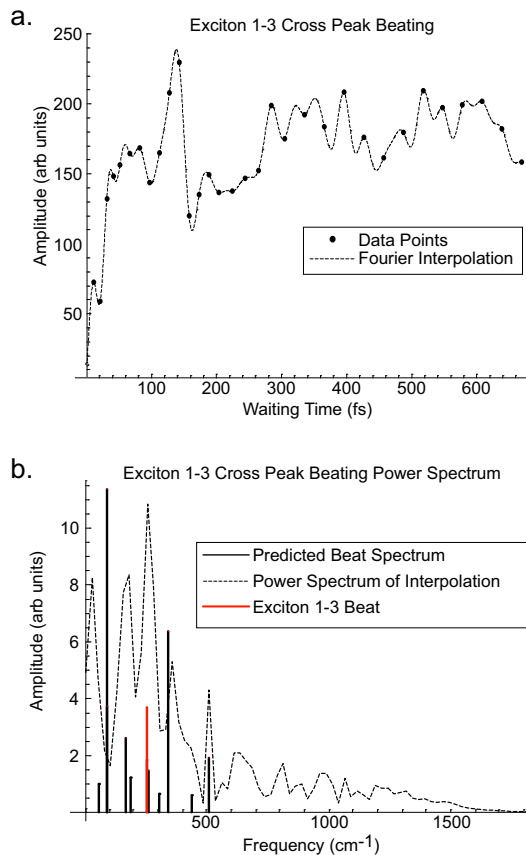


Figure 3.5: (a) The raw amplitude of the exciton 1-3 cross-peak, with a Fourier interpolation of the points (dotted line). (b) The power spectrum of this interpolation (dotted line), the exciton beating line spectra of both excitons 1 and 3 (black), and the 1-3 beat frequency (red). We expect that the other frequencies may couple to this cross-peak but that the dominant frequency corresponds to the red transition. The apparent low-frequency peak is due to the growth of the cross-peak amplitude and appears as a peak because the data were demeaned (mean subtracted from the data) before the transform to improve numerical accuracy, pinning the zero frequency component to zero.

complexes do not depend on dephasing of the ensemble properties observed in a measurement. In an ensemble sense, the presence of quantum coherence means that the mean square displacement of the initial excitation from a quantum walk increases quadratically with time rather than linearly as in diffusive hopping of excitation.⁷³

But a more microscopic picture of the implications of such quantum coherence for energy transfer can be found by considering an individual complex: superposition states formed during a fast excitation event allow the excitation to reversibly sample relaxation rates from all component exciton states, thereby efficiently directing the

energy transfer to find the most effective sink for the excitation energy (which, in the isolated FMO complex, is the lowest energy state). When viewed in this way, the system is essentially performing a single quantum computation, sensing many states simultaneously and selecting the correct answer, as indicated by the efficiency of the energy transfer. In the presence of quantum coherence transfer, such an operation is analogous to Grover's algorithm, with the Hamiltonian describing both relaxation to the lowest energy state and coherence transfer (refilling the coherence lost from the transfer to the lowest energy state);⁷⁴ such a scheme can provide efficiency beyond that of a classical search algorithm. This mechanism contrasts with a semiclassical 'hopping' mechanism through which the excitation moves stepwise from exciton state to exciton state, dissipating energy at each step, which would be similar to a classical search where only one state can be occupied at any one time. Such a mechanism also raises the possibility of non-local events, although more detailed analysis is needed before we can determine whether such effects are present in FMO.

3.5 Conclusions

The FMO light-harvesting complex provides an opportunity to apply more complete energy transfer theories that invoke non-Markovian dynamics and include coherence transfer. Such theories need to include wavelike energy motion owing to long-lived coherence terms, alongside the population transfer included in current models. Further, the observed preservation of coherence in this photosynthetic system requires us to redefine our description of the role of electron-phonon interactions within photosynthetic proteins. In particular, the protein may not only enforce the structure that gives rise to the couplings, but also modulate those couplings with motions of charged residues and changing local dielectric environments, which will change exciton energies and promote coherence transfer.

Chapter 4

Quantum Coherence Enabled Determination of the Energy Landscape in Light-Harvesting Complex II

Adapted with permission from *Journal of Physical Chemistry B*, **113**, 16291-16295 (2009). Copyright 2009 American Chemical Society.

The near-unity efficiency of energy transfer in photosynthesis makes photosynthetic light-harvesting complexes a promising avenue for developing new renewable energy technologies. Knowledge of the energy landscape of these complexes is essential in understanding their function, but its experimental determination has proven elusive. Here the observation of quantum coherence using two-dimensional electronic spectroscopy is employed to directly measure the fourteen lowest electronic energy levels in light harvesting complex II (LHCII), the most abundant antenna complex in plants containing approximately 50% of the world's chlorophyll. We observe that the electronically excited states are relatively evenly distributed, highlighting an important design principle of photosynthetic complexes that explains the observed ultrafast intracomplex energy transfer in LHCII.

4.1 Introduction

In the initial stages of photosynthesis, solar energy is absorbed by and transferred through intricate networks of pigment-protein complexes with unrivaled speed and efficiency. The key to understanding how these complexes function, and the proposed modulation of the function,⁷⁵⁻⁷⁷ lies in the relationship between the spatial organi-

zation of their pigments and the resulting excited-state potential energy surfaces. In almost all photosynthetic complexes, however, the excitons composing this energy landscape are so closely spaced that they become indiscernible in the linear absorption spectrum, even at cryogenic temperatures. This spectral congestion has meant that assignment of electronic energy levels is indirect, based on extensive modeling in combination with multiple forms of spectroscopy.^{75,78}

In the study of photosynthetic complexes, much attention has recently been paid to the role of quantum coherences, coherent superpositions of excitons that can be prepared when a broadband light pulse excites the system.^{8,21,25,79,80} Quantum coherence in a photosynthetic system was first observed in the Fenna-Matthews-Olson complex^{8,29} and has been discussed as an integral component of highly efficient photosynthetic light-harvesting.^{8,9,21,79,80} If we describe the evolution of these electronically excited complexes by the time progression of the density matrix for a two-level system as shown in Eq. 1.2, it can be seen that excitonic coherences evolve with a phase factor associated with the energy difference between the two participating excitons. Two-dimensional spectroscopy measures this phase evolution which manifests itself as an oscillation in the amplitude of the peaks in 2D spectra.^{25,26} Therefore, while spectral broadening effects may prohibit resolution of individual excitons, each exciton contribution buried within a broad peak oscillates with a unique pattern. The excitons' characteristic beating frequencies, combined with the ability of two-dimensional spectroscopy to specifically probe coherence contributions to the signals, provide a method by which the individual excitons can be precisely located.

4.2 Methods

4.2.1 Sample Preparation

LHCII trimers were isolated from *Arabidopsis thaliana* as previously published⁸¹ and dissolved in a Hepes buffer pH = 7.6 with the detergent, n-dodecyl α -D-maltoside 0.06%. The sample was then mixed with glycerol, 30:70 v/v, placed in a 200 μ m quartz cell, and cooled to 77 K. A sample absorbance of 0.14 was measured at 675 nm.

4.2.2 2D Electronic Spectroscopy

The 2D electronic spectroscopy experiment^{23,24,52,82} and apparatus^{24,29} have been described in detail elsewhere. A home-built Ti:sapphire oscillator seeded regenerative amplifier⁶² pumped a home-built non-collinear optical parametric amplifier to produce the spectrum given by the red trace in Fig. 2.2 with 80 nm of bandwidth centered at 640 nm. Prism pair compression enabled 18 fs pulse duration, as measured by autocorrelation. The beam was split to produce three pulses (6 nJ) separated by

two time delays, coherence time (τ) and waiting time (T), and a weak local oscillator. These four beams were focused in a box geometry to a spot size of less than 100 μm at the sample position. The signal field proportional to the resulting third-order polarization is heterodyne-detected and spectrally-resolved in a given phase-matched direction. The coherence time, τ , is scanned from negative to positive time at a fixed waiting time, and Fourier transformation along the τ axis produces a 2D spectrum.

The 2D spectrum provides a map that correlates the excitation and emission frequencies of the sample: the peaks along the diagonal correspond to those in the linear absorption, and off-diagonal features, “cross peaks”, arise from electronic coupling between pigments and energy transfer between excitons. Furthermore, excitonic quantum coherence manifests itself as oscillations in the amplitude of diagonal and cross peaks as a function of T . In congested spectra where excitons are closely spaced energetically, cross peaks will appear near their diagonal counterparts. As a result, oscillations in the amplitude of cross peaks can interfere with those of the peaks directly on the diagonal, making it extremely difficult to isolate individual coherence contributions in conventional 2D spectra. Recently, we have shown that only diagonal signals arising from quantum coherences appear in nonrephasing 2D spectra allowing them to be analyzed free from interference of beating cross peaks.²⁶ Nonrephasing spectra include data from only negative coherence time contributions, where the time ordering of the first two pulses is reversed.

Evolution of the diagonal cut of the nonrephasing 2D spectra as a function of waiting time, T , thus provides a means to specifically probe the coherent phase evolution of superpositions of excitons prepared by the first two laser pulses in the experiment. A Fourier-transform with respect to T resolves the frequencies of the coherence oscillations to yield a power spectrum of these beat frequencies vs. exciton energies. Each peak on this coherence power spectrum can be assigned specifically to a coherence density matrix element (Eq. 1.2). In an energetically disordered system, each exciton can participate in multiple coherences with other excitons in the system. This leads to a pattern of beat frequencies unique to each exciton whose peaks in the power spectrum line up along the same exciton energy, indicating the exciton’s position and permitting direct measurement of the energy landscape. Furthermore, a coherent superposition of two excitons gives rise to a pair of “mirror peaks” that appear at the same beat frequency and the respective energies of the two contributing excitons, which can be useful in assigning excitons with low oscillator strength. If only one mirror peak is detected in the power spectrum, the location of the second exciton can be estimated from the energy of the first exciton and the beat frequency.

4.2.3 Simulations

Simulated coherence power spectra were generated from LHCII trimer Hamiltonians. The Hamiltonian used for Figs. 4.4c and 4.5c was constructed from previously published trimeric site energies⁷⁵ and couplings provided by V. I. Novoderezhkin that

were calculated using the ideal dipole approximation (IDA). The magnitudes of the couplings used in the Hamiltonian that generated Figs. 4.4*b* and 4.5*b* were calculated by the transition density cube method (TDC) by Frähmcke and Walla⁸³ while signs were assigned from the IDA values.⁷⁵ The site energies of the Hamiltonian for Figs. 4.4*b* and 4.5*b* were optimized to match the experimental data. The ratio of Chl*b* to Chl*a* dipole strengths was 0.853⁸³ and all of the one-exciton transition dipoles were scaled by the experimental laser spectrum. The relative peak amplitudes in the theoretical power spectrum were calculated using orientationally averaged response magnitudes^{61,71,72} for the associated nonrephasing pathways.²⁶ Pathways containing two-exciton transitions were not included, because monomer simulations (not shown) revealed that they do not contribute significantly, most likely due to the relatively weak one- to two-exciton transition dipole moments. Both effects were assumed to be negligible in the calculation of the beat frequencies, but the exciton energies used were those calculated by Novoderezhkin et al.⁷⁵ (Figs. 4.4*c* and 4.5*c*) or determined in this work (Figs. 4.4*b* and 4.5*b*). In the theoretical modeling of coherence power spectra, all peaks were dressed with Gaussian distributions along both axes to simulate homogeneous and inhomogeneous broadening effects.

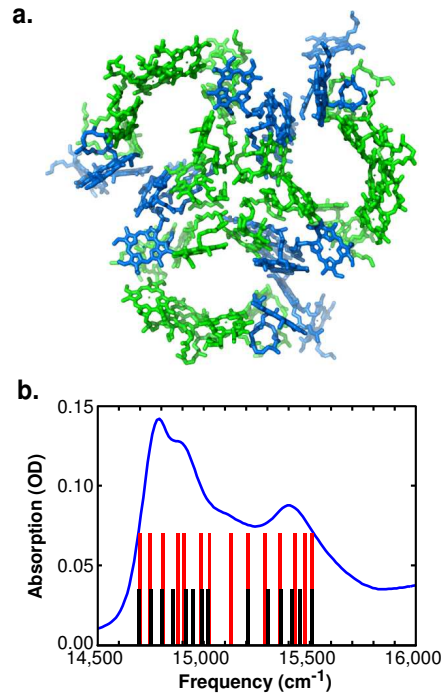


Figure 4.1: (a) Chlorophyll arrangement in LHCII trimer with Chl*a* and Chl*b* shown in green and blue, respectively.⁸⁴ (b) Linear absorption spectrum of LHCII trimers at 77 K. Red sticks indicate the exciton energies determined in this experiment while black sticks are previously predicted values.⁷⁵

4.3 Results and Discussion

We have applied the technique discussed above to investigate coherence evolution of excitations in LHCII, the major light-harvesting complex in plants. The trimeric x-ray crystal structure of LHCII was determined at high resolution,^{6,84} showing that each protein monomer contains 14 chlorophyll molecules with two spectral variants: eight chlorophyll *a* (Chl*a*) molecules, producing an absorption band from 14,500 cm^{-1} to 15,000 cm^{-1} , and six chlorophyll *b* (Chl*b*) molecules, giving rise to an absorption peak at 15,500 cm^{-1} (Fig. 4.1*a*). Even at 77 K, the 14 lowest energy (Q_y) electronic transitions arising from the chlorophyll molecules cannot be distinguished in the linear absorption spectrum (Fig. 4.1*b*). This congestion is extended to the 2D relaxation spectrum, shown in Fig. 4.2*a* for $T = 250$ fs, where the diagonal features correspond to those in the linear absorption. Energy transfer from Chl*b* to Chl*a* as well as relaxation within the Chl*a* region can be seen in the 2D relaxation spectrum via strong cross peaks below the diagonal while the negative features above the diag-

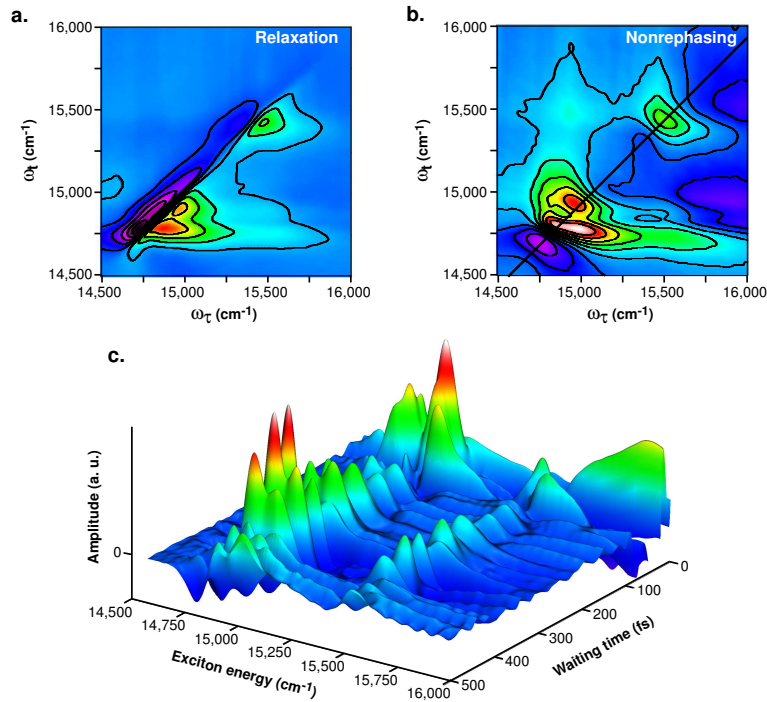


Figure 4.2: (a) The real part of a representative 2D relaxation spectrum for $T = 250$ fs. (b) The real part of the nonrephasing 2D spectrum for $T = 250$ fs. (c) The amplitude of the diagonal cut of the nonrephasing 2D spectra as a function of waiting time. For the purposes of presentation, a cubic spline interpolation connects the data points that were acquired in 10 fs increments. For (a)-(c), amplitude increases from purple (negative) to white (positive).

onal arise from excited state absorption (ESA) to the large manifold of two-exciton states. The corresponding nonrephasing 2D spectrum in Fig. 4.2b has characteristic “phase-twisted” lineshapes^{26,82} and comparatively enhanced cross peaks as the strong, stationary signal along the diagonal from rephasing pathways has been removed. While the nonrephasing lineshape has been shown to increase resolution along the diagonal,⁸⁵ it is clear in Fig. 4.2b that this enhancement alone is not sufficient to isolate the 14 individual contributions to the diagonal signal.

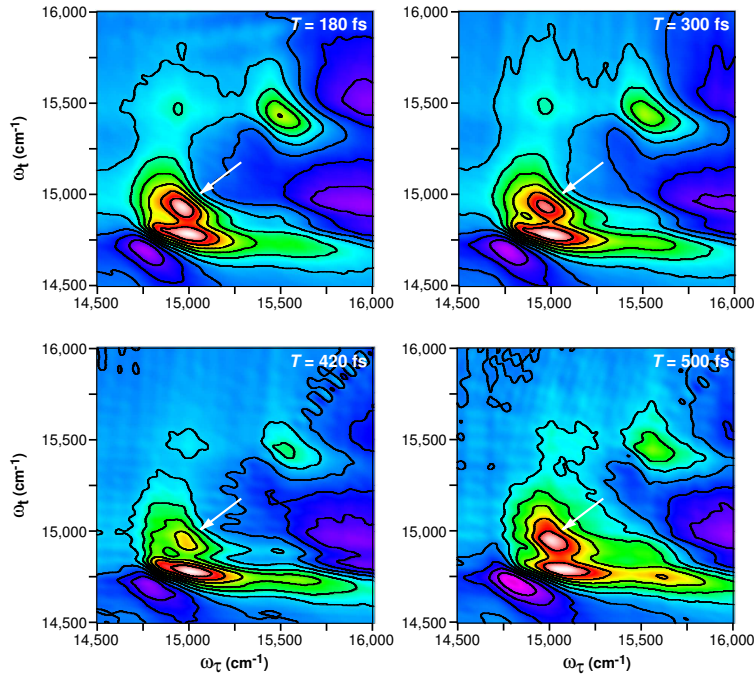


Figure 4.3: The real parts of selected 2D nonrephasing spectra of LHCII are shown for waiting times between $T = 0$ fs and $T = 500$ fs to illustrate quantum beating of the diagonal features. The high energy Chla peak (white arrows) can be seen in different stages of oscillations throughout the duration of the experiment. All spectra are shown normalized to their maximum value.

To resolve the oscillations in spectral amplitude arising from electronic coherences in LHCII, spectra were collected for waiting times from 0 to 500 fs in 10 fs steps. Selected nonrephasing 2D spectra are shown in Fig. 4.3 where the relative amplitudes of the diagonal features visibly oscillate, indicative of coherence quantum beating. Figure 4.2c shows the amplitude along the diagonal of the nonrephasing 2D spectra as a function of waiting time, where the exciton energy axis denotes the diagonal frequency in the 2D spectra. Quantum beating is clearly observed in both Chla and Chlb regions. As seen in other photosynthetic complexes,⁸ the coherence is long-lived in LHCII with the quantum beating lasting beyond the 500 fs scan of the experiment

and beyond the lifetimes of many excitons in the system,⁷⁵ suggesting this to be a general phenomenon. This result supports the speculation that evolution has designed these complexes to preserve coherence; a feat likely achieved through strongly correlated protein environments.^{9,31,86,87} Recent studies suggest that such long-lived coherence is instrumental in facilitating extremely efficient energy transfer.^{8,21,79,80}

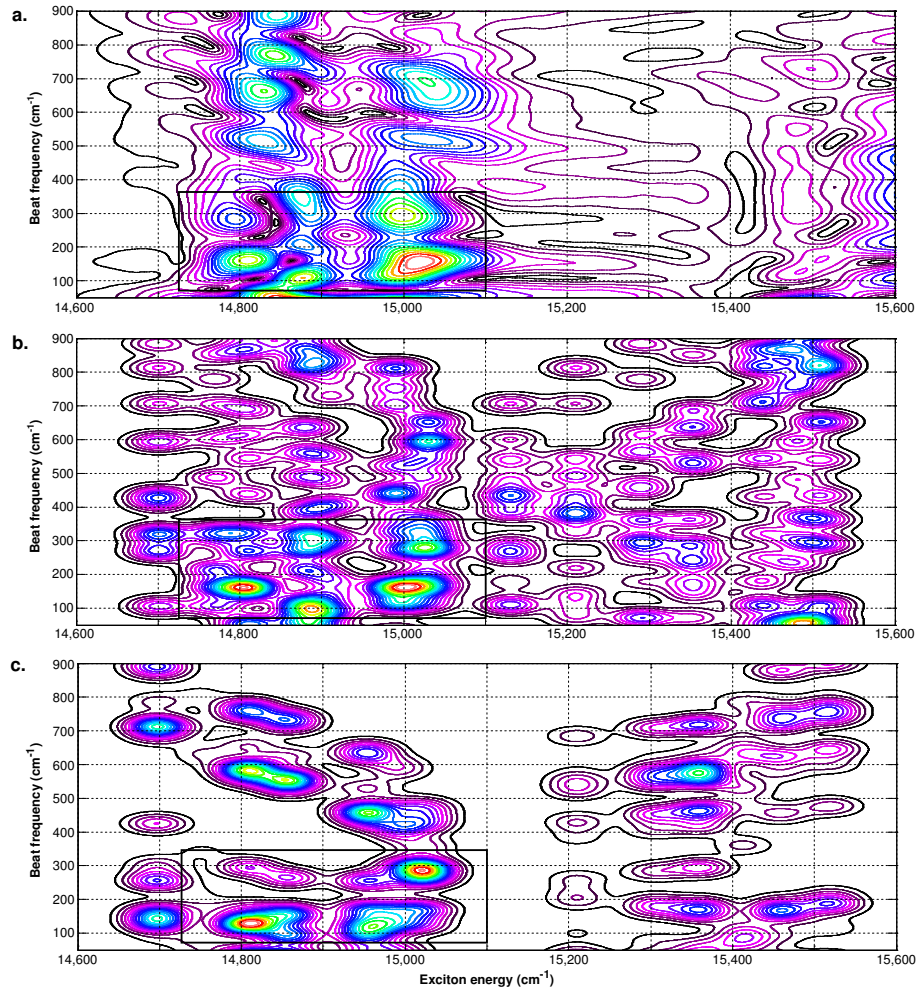


Figure 4.4: Power spectra of quantum beating in LHCII constructed from experimental 2D data (*a*) and theoretical simulations from the new model (*b*) and the model in ref. 75 (*c*) as described in the text. The beat frequency axis begins at 50 cm^{-1} to remove the strong DC component and contours are placed at 5% intervals. The boxes indicate the regions examined in detail in Fig. 4.5.

Figure 4.4*a* shows the LHCII coherence power spectrum obtained by Fourier transforming the diagonal amplitude of nonrephasing 2D spectra (Fig. 4.2*c*) along the waiting time axis. Clearly, the peaks in the power spectrum align vertically, indicating locations of the exciton levels. Figure 4.5*a* shows an expanded view of the Chl*a*

region denoted by the box in Fig. 4.4a. The circled peak with an exciton energy of $14,800\text{ cm}^{-1}$ and a beat frequency of 150 cm^{-1} has a distinct low energy wing (arrow) that indicates the position of an exciton with slightly lower energy causing a slightly lower beat frequency peak. This feature illustrates how this experimental technique can utilize individual beat frequency patterns to separate energetically similar excitons. Furthermore, as the beat frequencies of the coherences experience

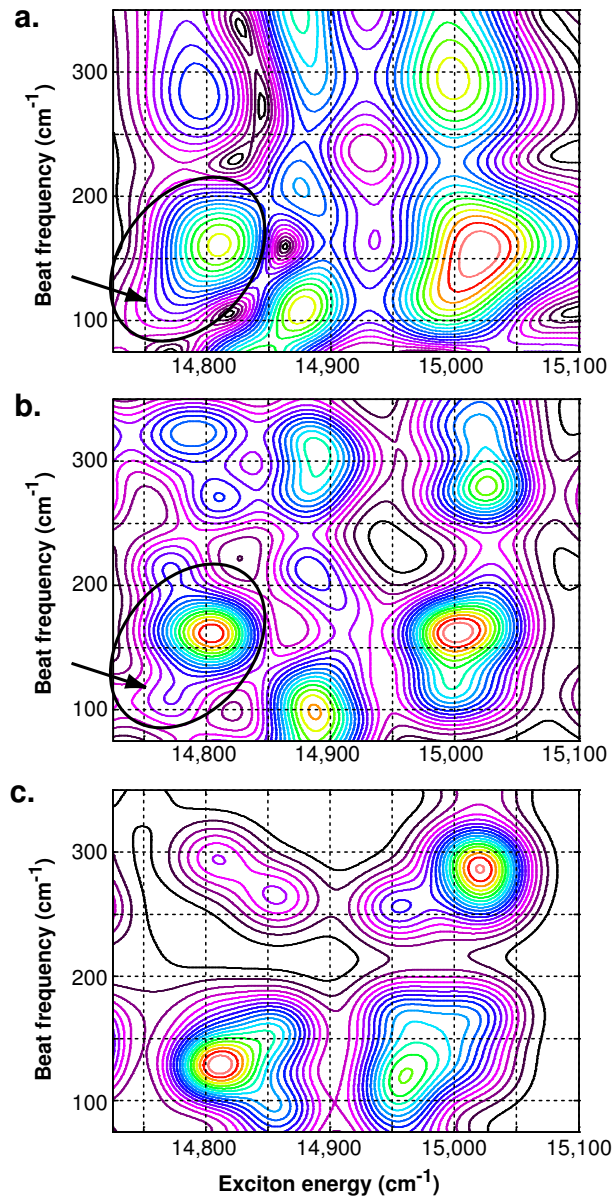


Figure 4.5: The boxed Chla regions of the power spectra in Fig. 4.4. The circled peak and arrow highlight features discussed in the text.

relatively weak bath effects, simulation of the power spectrum presents us with the unique opportunity to directly access the system’s electronic Hamiltonian. Our initial comparison with the experimental data was done with the coherence power spectrum calculated from the Hamiltonian developed for an LHCII trimer by Novoderezhkin et al.⁷⁵ The comparison is shown in Table 4.1 and graphically Figs. 4.4 and 4.5 where (a) are the experimental spectra and (c) are the spectra generated from the previously published Hamiltonian.⁷⁵ While there is considerable qualitative agreement between experiment and the model, there were significant differences in exciton position and peak amplitude. Therefore, we developed a new model based on couplings calculated by Frähmcke and Walla⁸³ and site energies that were adjusted to give better agreement with the data. Figure 4.4b displays the coherence power spectrum calculated by our new model; it is important to note that because $\text{Ch}l_b \rightarrow \text{Ch}l_a$ relaxation effects⁸⁸ are not included, features arising from coherences involving primarily $\text{Ch}l_b$ excitations appear artificially stronger in the simulations. Figure 4.5b zooms in on the $\text{Ch}l_a$ region for a detailed comparison to experiment, in which it can be seen that all of the features’ positions and amplitudes are well reproduced. Clearly, simulation of the coherence power spectrum provides a stringent test for models of pigment-protein complexes, enabling better refinement of theoretical models.

Analysis of the entire experimental power spectrum yields the exciton energies in Table 4.1. Excitons 9 and 10 have very low oscillator strength in the experimental

exciton	experimental energy (cm^{-1}) ^a	theoretical energy (cm^{-1}) ^b
1	14700	14699
2	14770	14751
3	14810	14804
4	14880	14858
5	14910	14918
6	14990	14952
7	15030	14992
8	15130	15022
9	15210	15210
10	15290	15306
11	15360	15363
12	15430	15416
13	15480	15456
14	15510	15512

^aPresent work. Exciton energies over 30 cm^{-1} higher than theoretical predictions are highlighted in boldface. ^bFrom ref. 75.

Table 4.1: Exciton energies determined from the 2D electronic spectroscopy experiment compared with those calculated from previous models

data and their positions were largely determined from several mirror peaks. This is consistent with previous modeling efforts in which excitons on the red edge of the Chl*b* band have been predicted to be “dark”.⁷⁸ The most striking difference in Table 4.1 between the experiment and previous model is the higher energy positions of excitons 6-8, the three highest energy excitons in the Chl*a* region. Of specific interest is the location of exciton 8 shown by the peak at an exciton energy of 15,130 cm^{-1} and a beat frequency of $\sim 400 \text{ cm}^{-1}$ in the experimental power spectrum (Fig. 4.4*a*); this same region in the simulated spectrum from the Novoderezhkin et al.⁷⁵ (Fig. 4.4*c*) is devoid of any features. Exciton 8 is thus located in the intermediate region of the spectrum where none had been predicted previously, yet almost exactly at the position of a weak shoulder on the blue edge of the Chl*a* linear absorption. This may explain why unique dynamics are observed in LHCII when pumping at this energy.⁸⁹

The experimentally-determined LHCII exciton energies reveal a reduction of the energetic gap between the Chl*b* and Chl*a* bands compared to previous assignments, resulting in a more evenly spaced energetic surface. This suggests that spacing between energy levels in LHCII may be tuned to match phonon frequencies of the surrounding proteins to optimize the efficiency of energy transfer since it is these vibrational modes that dissipate excess energy during exciton relaxation. The energy gap between Chl*b* and Chl*a* bands in LHCII was previously predicted⁷⁵ to be approximately 190 cm^{-1} , while studies of chlorophyll-protein complexes found that few protein vibrational modes in that region are strongly coupled to the chlorophylls’ Q_y excited states.⁹⁰ The rate of energy transfer between Chl*b* and Chl*a* bands, however, has previously been observed to occur on a sub-picosecond timescale with an extremely rapid 150-300 fs component.⁸⁹ While multivibrational quanta transitions are expected to play a large role in the slower interband relaxation rates,⁹¹ this fastest rate is likely dominated by single quantum transitions requiring a smaller energetic gap. The density of vibrational modes near 100 cm^{-1} , closer to the energetic gap found in this study, is more than twice as large as that for 190 cm^{-1} ,⁹⁰ thereby facilitating Chl*b* to Chl*a* energy transfer. The reduced spacing between Chl*a/b* bands revealed in this work could therefore explain the most rapid interband energy transfer in the LHCII.

4.4 Conclusions

Two significant applications of the coherence power spectrum technique described here seem apparent. There is substantial evidence that photosynthetic complexes change their structural conformation, and hence their energy landscape, in vivo to create dramatic changes in their function; for example, allowing the same complex to transfer excitation efficiently in low light conditions and to dissipate excess energy in high light.^{76,92} Application of this technique to structurally similar photosynthetic complexes that exhibit switchable functions, such as the photosystem II minor com-

plexes,^{77,92} should provide insight into how nature has achieved this adaptive versatility. Second, the technique described here represents a significant step towards the determination of the full density matrix of molecular complexes, i.e. quantum state tomography.⁹³ Each of the peaks in Fig. 4.4*a* corresponds directly to an individual off-diagonal element in the system's density matrix weighted by the appropriate dipole factors. If the dipole factors are known, such plots could be used to experimentally evaluate, for example, entanglement witnesses and determine the role of non-local behavior in photosynthetic light-harvesting.

Chapter 5

Vibrationally-Mediated Dynamics in β -carotene Probed with Broadband 2D Electronic Spectroscopy

5.1 Introduction

Despite the ubiquitous presence of carotenoids in natural systems, and almost four decades of research, the electronic structure of these polyenes is still intensely debated.^{14,34} The ultrafast internal conversion from the optically bright S_2 state to the lower energy, optically ‘dark’ (i.e., the transition is not allowed in one-photon absorption from S_0) state, S_1 , is proposed to be mediated by a conical intersection.⁹⁴ However, controversy surrounds the existence and role of other dark states lying energetically intermediate to S_2 and S_1 .^{33,34} The unique ability of two-dimensional (2D) spectroscopy to resolve emission as a function of excitation wavelength makes it an ideal tool to study carotenoids such as β -carotene.

5.2 Methods

The theory and apparatus for 2D FT electronic spectroscopy have been described in detail elsewhere.²⁴ Briefly, a non-collinear optical parametric amplifier (NOPA), pumped by 800 nm pulses from a Ti:sapphire oscillator/regenerative amplifier system, produces the broadband laser spectrum given by the green trace in Fig. 2.2. The pulses are subsequently compressed via the adaptive, diffraction-based SLM pulse shaper⁴⁶ described in Chapter 2 before being split into three successive pulses that are focused onto the sample in a box geometry. The signal that emerges in the desired phase-matched direction is spectrally-resolved and heterodyne-detected. The

time delay between pulses 1 and 2, the coherence time (τ), is varied for each waiting time (T), the time between pulses 2 and 3. The resulting interferograms for a given T are Fourier-transformed along the τ axis to produce the final 2D spectrum. This 2D relaxation spectrum is composed of free-induction decay (nonrephasing) and photon-echo (rephasing) signals. Spectra were collected for $T = 0, 10, 20, 30, 40, 50, 60, 70, 80, 90, 100, 110, 120, 130, 140, 150, 175, 200, 225, 250, 275, 300, 325, 350, 375, 400, 425, 450, 475, 500, 550, 600, 650, 700, 750, 800, 1000, 2000, 3000, 4000, 5000, 7500, 10000,$ and 20000 fs.

The 12 fs pulses used in this experiment were centered at 550 nm with a FWHM of 70 nm to excite the lowest energy $S_0 \rightarrow S_2$ transition of β -carotene and monitor the $S_1 \rightarrow S_n$ excited state absorption (ESA). All experiments were performed at 77 K to narrow the spectral features allowing overlapping signals to be separated. The cryogenic temperature also reduces the heterogeneous distribution of isomers that have been implicated in the presence of different kinetics for intermediate electronic states.⁹⁵ While 2D electronic experiments have been performed previously on β -carotene,⁹⁶ the resolution afforded by the low temperature and increased spectral bandwidth in the current study allow the electronic character of this important system to be examined in unprecedented detail.

5.3 Results and Discussion

While analysis of these results is ongoing, initial observations have already revealed several features that have no experimental precedent and deviate from what is known or expected for these systems and electronic 2D spectroscopy. For the first time we are able to resolve cross peaks as early as $T=20$ fs as well as uncharacteristic and dynamic lineshapes. To explore the origins of these features, we begin by discussing the long time dynamics, where we define “long time” as occurring after the S_2 lifetime.

5.3.1 Long Time Dynamics

Figure 5.1a shows the real part of the 2D relaxation spectrum for β -carotene in 2-methyltetrahydrofuran (2-mTHF) at $T=325$ fs. The positive peak on the diagonal is the remaining $S_0 \rightarrow S_2$ bleach following the excitation of S_2 . The $S_1 \rightarrow S_n$ ESA at ~ 575 nm appears as the strong negative peak below the diagonal after internal conversion from S_2 . Between these two expected peaks, multiple features are present. Negative signals in this energetically intermediate region have been previously observed in transient absorption studies and assigned to either a hot ground, S_0 ,⁹⁷ or new excited state, S^* .^{95,98} From the 2D spectra, however, it appears that multiple transitions give rise to signals in this region with both positive and negative contributions. For the transition nearest in energy to the S_1 ESA, highlighted by the boxed region in Fig. 5.1a, this is especially apparent in the rephasing contribution to the 2D signal as

shown in Fig. 5.1*b*. Here the transition displays the diagonal lineshape characteristic of rephasing signals, but has a phase shift across the peak similar to a dispersive signal as opposed to a purely positive or negative peak expected for real, absorptive 2D spectra.⁹⁹ Although “absorptive” and “dispersive” are no longer strictly correct when discussing features of the rephasing and nonrephasing portions of the 2D signal separately, we will continue to use these terms to describe the characteristic lineshapes associated with them.

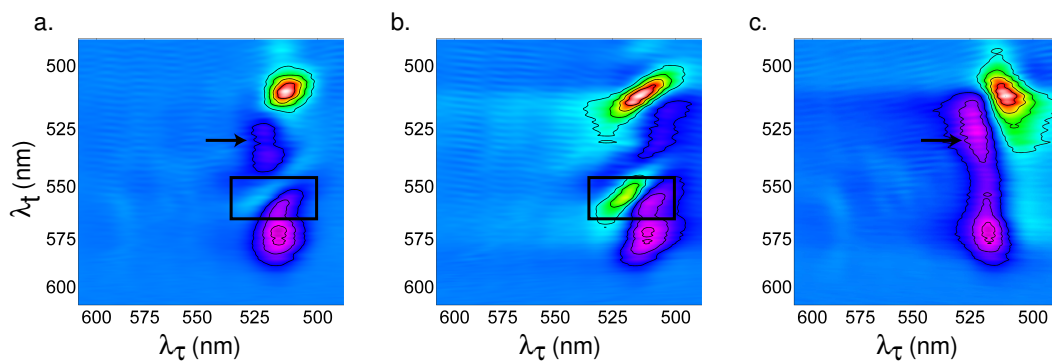


Figure 5.1: Representative real 2D (*a*) relaxation, (*b*) rephasing, and (*c*) nonrephasing spectra for β -carotene in 2-mTHF at long times ($T=325$ fs). The feature in the boxed region exhibits a lineshape characteristic of coupling to a high energy vibrational mode. The black arrow points to a cross peak near the diagonal that arises from the nonrephasing signal. Amplitude increases from purple (negative) through blue (zero) to white (positive).

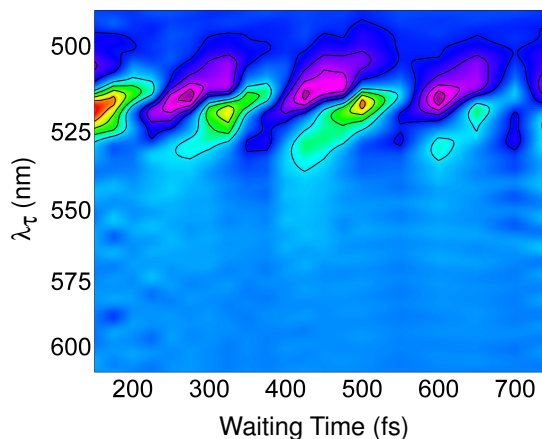


Figure 5.2: Cuts of the real 2D rephasing spectra for $\lambda_t=555$ nm showing the oscillating phase of the lineshape of the transition in the boxed region in Fig. 5.1.

A dispersive lineshape for a real, rephasing cross peak such as in Fig. 5.1b has been observed in recent theoretical work and is indicative of coupling between the electronic transition and a high energy vibrational mode.^{27,28} In addition, the modeling efforts go on to predict that the phase of the peak can oscillate as a function of T .^{27,28} To investigate this dynamic behavior, a cut of the rephasing 2D spectrum for $\lambda_t=555$ nm is plotted as a function of T in Fig. 5.2 and the phase oscillation of the lineshape is evident. It is important to note that dynamics resulting from fast vibrational modes are highly dependent on the laser spectrum,²⁷ and as such, the resolution of this characteristic lineshape is only possible with an ultrabroadband spectrum such as that used in this experiment.

At this point we are unable to assign this vibrational coherence to existing on the S_0 or S_1 surface unambiguously. While the theoretical efforts model two-level systems making them more analogous to a coherence on the ground state, they predict this behavior in the presence of multiple diagonal peaks^{27,28} not observed in our data. Furthermore, the fact that the dispersive nature of the lineshape becomes apparent on a timescale associated with the S_2 lifetime suggests decay from this state is necessary before the coherence is observable. For the vibrational coherence to exist on the S_1 surface, the wavepacket would have to survive the decay from S_2 which would require coupling between these surfaces and a corresponding curve crossing consistent with the ultrafast relaxation. Transient grating experiments by Sugisaki *et al.* have indicated, however, that any vibronic coherence present on the S_2 surface after excitation decays almost instantaneously.¹⁰⁰ These findings were supported by quantum control experiments.¹⁰¹

While the feature attributed to vibrational coherence is only present in rephasing spectra, there are also nonrephasing signals in this intermediate region at long times. The black arrow in Fig. 5.1c points to a cross peak just below the diagonal that is only evident in the nonrephasing spectrum. Like the rephasing cross peak, it exhibits a dispersive lineshape; however, the lineshape of this feature is not observed to change as a function of T . The origin of this peak is still under investigation, but it may be related to a positive signal in this region observed at short times as discussed in the next section.

5.3.2 Short Time Dynamics

The 12 fs time resolution of our experiment allows the early dynamics in β -carotene to be followed as the excitation propagates along the S_2 surface. The relaxation, rephasing, and nonrephasing 2D spectra for β -carotene in 2-mTHF at $T=20, 30,$ and 40 fs are given in Fig. 5.3. In the rephasing signal for short times, there is a strong cross peak apparent by $T=20$ fs, the first waiting time collected outside of pulse overlap. Integration of this area of the 2D spectra, as indicated by the box in Fig. 5.3, as a function of waiting time reveals beating only in the rephasing signal with a period of ~ 20 fs during the S_2 lifetime (Fig. 5.4). Assignment of this peak remains

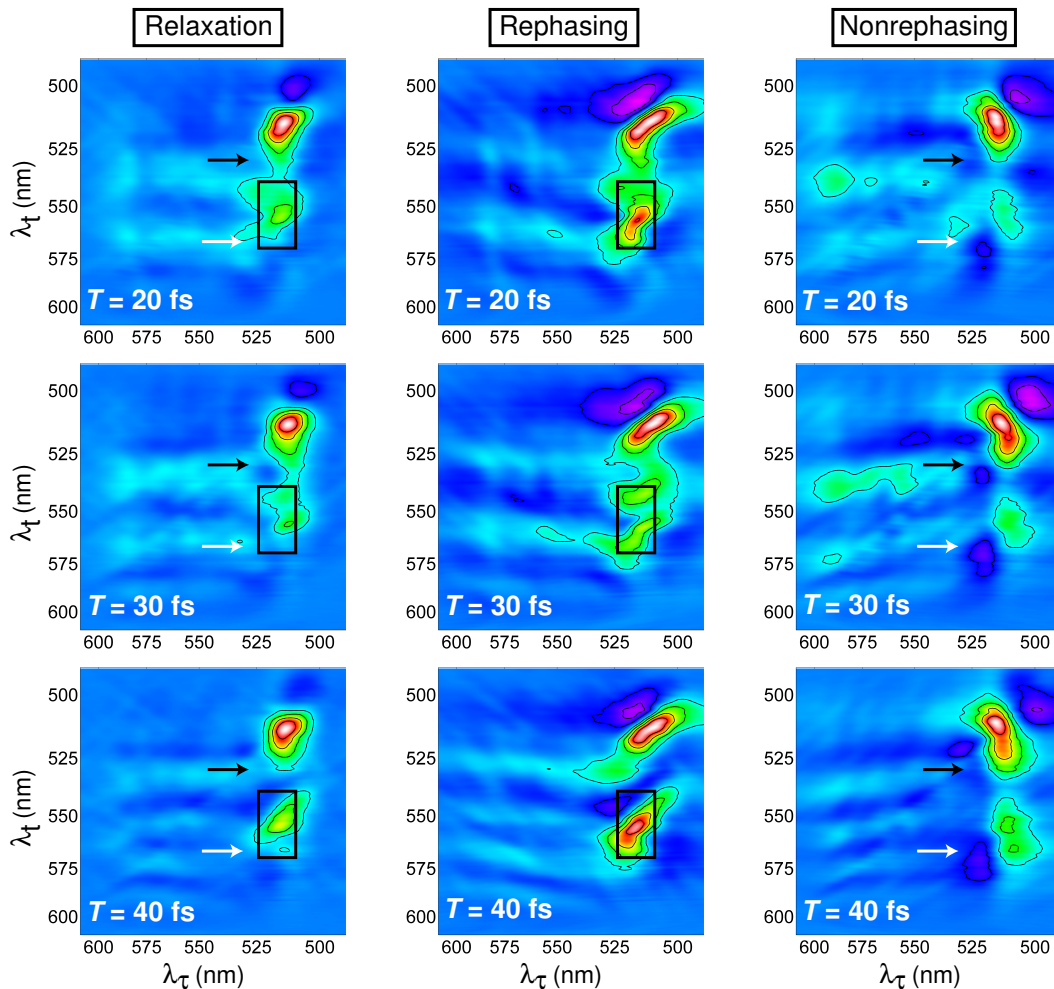


Figure 5.3: Representative spectra of the short time dynamics observed for (*left*) relaxation, (*middle*) rephasing, and (*right*) nonrephasing signals from β -carotene in 2-mTHF. The white and black arrows highlight nonrephasing features discussed in the text while the dynamics in the boxed region are presented in Fig. 5.4.

elusive. Given its appearance in only rephasing pathways at short times (compare the top panels in Fig. 5.3) requires a signal arising from a coherence during the waiting time.²⁶ An electronic coherence would require excitation of the second pulse to a different electronic state than S_2 ; however, the lack of a corresponding diagonal peak at the emission energy makes this unlikely. Ostroumov *et al.* assigned quantum beats they observed in transient absorption studies of β -carotene to an electronic coherence between S_2 and an electronic dark state with symmetry $1B_u^-$.¹⁰² The existence of this state is still debated.³⁴ Assignment of this cross peak to a vibrational coherence also reveals inconsistencies when compared with theoretical predictions. The off-diagonal

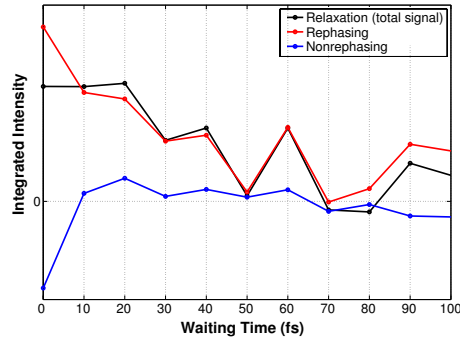


Figure 5.4: Integrated regions of 2D spectra indicated by the box in Fig. 5.3 showing clear beating in the amplitude of the rephasing cross peak.

position of this cross peak suggests coupling to a vibrational mode of $\sim 1000 \text{ cm}^{-1}$. As discussed in the previous section, theoretical models suggest such beating should be accompanied by changes in the lineshape,²⁷ which are not experimentally observed for this feature.

Two cross peaks below the diagonal are observed in the nonrephasing spectra at short times. The first is a positive peak that grows in just below the diagonal highlighted by the black arrow in Fig. 5.3. This feature is in a similar position to the nonrephasing cross peak observed at long times (black arrow in Fig. 5.1), however, the lineshape is different appearing absorptive at short times and dispersive at long times. Unlike the rephasing peak, this change in lineshape is not seen to oscillate.

The second nonrephasing cross peak at short times (white arrow in Fig. 5.3) appears in a similar position to the short time rephasing cross peak, but differences in the dynamics and lineshape suggest a different origin. Unlike the rephasing peak, the nonrephasing feature is not clearly above the noise until $T = 40 \text{ fs}$. In addition, it displays a dispersive lineshape and shows no significant oscillation in amplitude or lineshape as a function of T . Looking at the imaginary part of this signal (Fig. 5.5), provides more clarity on the dynamics. Here it can be seen that at short times, the signal in the region is associated with a single negative feature. This means that the signal observed in the real portion is associated with a single peak displaying a dispersive lineshape as opposed to two absorptive features of opposite sign. By $T=300 \text{ fs}$, this feature can be seen to slightly redshift in energy along the λ_t axis as its lineshape in the imaginary part of the signal has changed from absorptive to dispersive suggesting a change of phase arising from the material during the waiting time. There have been two independent theoretical treatments that have shown vibronic states giving rise to such changes in the material phase and hence the resulting lineshape;^{27,28} however this behavior is seen as oscillation of the lineshape as shown in the previous section, not as the seemingly irreversible lineshape change observed here.

One possible source of an irreversible change in the phase of the material is geo-

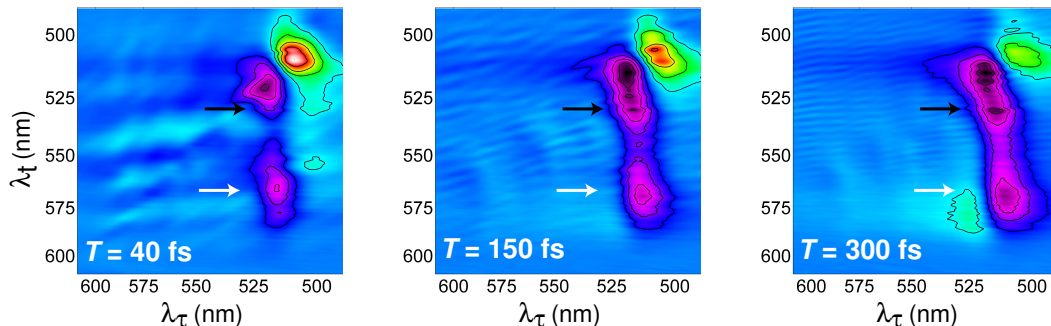


Figure 5.5: Representative imaginary, nonrephasing 2D spectra. The white and black arrows are in the same location as those in Fig. 5.3 and highlight the irreversible change in lineshape observed for both features.

metric phase.¹⁰³ Geometric phase may be acquired by a wavefunction as it circles a region that contains a conical intersection, a point of degeneracy between two electronic surfaces at which the Born-Oppenheimer approximation ceases to be valid. While the $S_2 \rightarrow S_1$ relaxation has been proposed to involve a conical intersection, its position and the related energetic barrier relative to the S_2 and S_1 minima remains unknown.⁹⁴ Previous photon echo studies of carotenoids have suggested the $S_2 \rightarrow S_1$ relaxation passes through a conical intersection¹⁰⁴ while more recent 2D experiments on β -carotene have been modeled assuming any conical intersection between the S_2 and S_1 surfaces is far from the region influencing the dynamics.⁹⁶ In an alternative view, S_2 and S_1 could be two minima on the same surface separated by a conical intersection with a higher lying surface. Relaxation from S_2 to S_1 would therefore acquire geometric phase as the wavepacket propagated around the intersection. In addition, the topography of the surface imposed by the presence of a conical intersection could steer the wavepacket based on its initial trajectory. This could explain the different photoproducts observed when exciting S_2 with excess energy.^{98,105} While no simulations have currently been done to directly show the effects of geometric phase on 2D spectra, the possibility is exciting and relevant for carotenoid systems.

Another explanation for the irreversible conversion from an absorptive lineshape to one of dispersive character, or vice versa, is that a peak with a dispersive lineshape grows in at later times overlapping the absorptive signal. The unequal weighting between positive and negative sides of the features suggests this may describe the observed behavior. From this perspective, the question of how a peak with a purely absorptive lineshape at all waiting times can appear in the imaginary part of a 2D spectrum (or a dispersive feature in the real part) remains unanswered. A more quantitative analysis of the kinetics is currently underway.

5.4 Conclusions

Two-dimensional electronic spectroscopy reveals multiple features energetically intermediate to the $S_0 \rightarrow S_2$ and $S_1 \rightarrow S_n$ transitions in β -carotene. The presence of signals with opposing phases in this region may explain the controversial assignments in the literature and suggests that dynamics here are more complex than expected from a single transition. Signals apparent at short times may arise from electronic coherences with “dark” states, while a feature at long times exhibits characteristics of coupling to high energy vibrational modes only observable with an ultrabroadband laser spectrum, such as used here. The origin of several of these features is still under investigation, but the dynamic nature of their lineshapes has not been experimentally observed previously, promising new insights into the energetic pathways in carotenoids.

Bibliography

- [1] Peumans, P.; Bulovic, V.; Forrest, S. R. *Appl. Phys. Lett.* **2000**, *76*, 2650–2652.
- [2] Scully, S. R.; McGehee, M. D. *J. Appl. Phys.* **2006**, *100*, 5.
- [3] Scholes, G. D. *J. Phys. Chem. Lett.* **2010**, *1*, 2–8.
- [4] Camara-Artigas, A.; Brune, D.; Allen, J. P. *Proc. Natl. Acad. Sci. USA* **2002**, *99*, 11055–11060.
- [5] Camara-Artigas, A.; Blankenship, R. E.; Allen, J. P. *Photosynth. Res.* **2003**, *75*, 49–55.
- [6] Standfuss, J.; van Scheltinga, A. C. T.; Lamborghini, M.; Kühlbrandt, W. *EMBO J.* **2005**, *24*, 919–928.
- [7] Wilk, K. E.; Harrop, S. J.; Jankova, L.; Edler, D.; Keenan, G.; Sharples, F.; Hiller, R. G.; Curmi, P. M. G. *Proc. Natl. Acad. Sci. USA* **1999**, *96*, 8901–8906.
- [8] Engel, G. S.; Calhoun, T. R.; Read, E. L.; Ahn, T. K.; Mančal, T.; Chung, Y.-C.; Blankenship, R. E.; Fleming, G. R. *Nature* **2007**, *446*, 782–786.
- [9] Lee, H.; Cheng, Y. C.; Fleming, G. R. *Science* **2007**, *316*, 1462–1465.
- [10] Calhoun, T. R.; Ginsberg, N. S.; Schlau-Cohen, G. S.; Cheng, Y. C.; Ballottari, M.; Bassi, R.; Fleming, G. R. *J. Phys. Chem. B* **2009**, *113*, 16291–16295.
- [11] Collini, E.; Wong, C. Y.; Wilk, K. E.; Curmi, P. M. G.; Brumer, P.; Scholes, G. D. *Nature* **2010**, *463*, 644–647.
- [12] Blankenship, R. E. *Molecular mechanisms of photosynthesis*; Blackwell Science: Oxford, 2002.
- [13] Kobayashi, M.; Akiyama, M.; Kano, H.; Kise, H. In *Chlorophylls and Bacteriochlorophylls*; Grimm, B., Porra, R. J., Rüdiger, W., Sheer, H., Eds.; Springer: New York, 2006; Vol. 25; pp 79–94.
- [14] Polívka, T.; Sundström, V. *Chem. Rev.* **2004**, *104*, 2021–2071.

- [15] van Amerongen, H.; Valkunas, L.; van Grondelle, R. *Photosynthetic excitons*; World Scientific: Singapore ; River Edge, N.J., 2000; Vol. Ch. 8. Exciton Dynamics.
- [16] Adolphs, J.; Müh, F.; Madjet, M.; Renger, T. *Photosynth. Res.* **2008**, *95*, 197–209.
- [17] Noy, D.; Moser, C. C.; Dutton, P. L. *BBA-Bioenergetics* **2006**, *1757*, 90–105.
- [18] Förster, T. *Ann. Phys. Leipzig* **1948**, *437*, 55–75.
- [19] Scholes, G. D. *Annu. Rev. Phys. Chem.* **2003**, *54*, 57–87.
- [20] Ishizaki, A.; Fleming, G. R. *Proc. Natl. Acad. Sci. USA* **2009**, *106*, 17255–17260.
- [21] Mohseni, M.; Rebentrost, P.; Lloyd, S.; Aspuru-Guzik, A. *J. Chem. Phys.* **2008**, *129*, 174106.
- [22] Chin, A. W.; Datta, A.; Caruso, F.; Huelga, S. F.; Plenio, M. B. *New J. Phys.* **2010**, *12*, 065002, 1367-2630.
- [23] Jonas, D. M. *Annu. Rev. Phys. Chem.* **2003**, *54*, 425–463.
- [24] Brixner, T.; Mančal, T.; Stiopkin, I. V.; Fleming, G. R. *J. Chem. Phys.* **2004**, *121*, 4221–4236.
- [25] Pislakov, A. V.; Mančal, T.; Fleming, G. R. *J. Chem. Phys.* **2006**, *124*, 234505.
- [26] Cheng, Y. C.; Fleming, G. R. *J. Phys. Chem. A* **2008**, *112*, 4254–4260.
- [27] Mančal, T.; Nemeth, A.; Milota, F.; Lukeš, V.; Kauffmann, H. F.; Sperling, J. *J. Chem. Phys.* **2010**, *132*, 184515.
- [28] Schubert, A.; Renziehausen, K.; Engel, V. *Phys. Rev. A* **2010**, *82*, 013419.
- [29] Brixner, T.; Stenger, J.; Vaswani, H. M.; Cho, M.; Blankenship, R. E.; Fleming, G. R. *Nature* **2005**, *434*, 625–628.
- [30] Panitchayangkoon, G.; Hayes, D.; Fransted, K. A.; Caram, J. R.; Harel, E.; Wen, J.; Blankenship, R. E.; Engel, G. S. *Proc. Natl. Acad. Sci. USA* **2010**, *107*, 12766–12770.
- [31] Müh, F.; Madjet, M. E. A.; Adolphs, J.; Abdurahman, A.; Rabenstein, B.; Ishikita, H.; Knapp, E. W.; Renger, T. *Proc. Natl. Acad. Sci. USA* **2007**, *104*, 16862–16867.

- [32] Ishizaki, A.; Calhoun, T. R.; Schlau-Cohen, G. S.; Fleming, G. R. *Phys. Chem. Chem. Phys.* **2010**, *12*, 7319–7337.
- [33] Hashimoto, H.; Yanagi, K.; Yoshizawa, M.; Polli, D.; Cerullo, G.; Lanzani, G.; De Silvestri, S.; Gardiner, A. T.; Cogdell, R. J. *Arch. Biochem. Biophys.* **2004**, *430*, 61–69.
- [34] Polívka, T.; Sundström, V. *Chem. Phys. Lett.* **2009**, *477*, 1–11.
- [35] Cerullo, G.; De Silvestri, S. *Rev. Sci. Instrum.* **2003**, *74*, 1–18.
- [36] Baltuška, A.; Fuji, T.; Kobayashi, T. *Opt. Lett.* **2002**, *27*, 306–308.
- [37] Vaswani, H. M. A Theoretical and Femtosecond Spectroscopic Investigation of Energy Transfer in Photosynthetic Complexes. Ph.D. thesis, University of California, Berkeley, 2005.
- [38] Kobayashi, T.; Baltuška, A. *Meas. Sci. Technol.* **2002**, *13*, 1671–1682.
- [39] Peil, J.; Riedle, E.; Gundlach, L.; Ernstorfer, R.; Eichberger, R. *Opt. Lett.* **2006**, *31*, 1289–1291.
- [40] Reid, G. D.; Wynne, K. In *Encyclopedia of Analytical Chemistry*; Meyers, R. A., Ed.; John Wiley & Sons: Chichester, 2000; pp 13644–13670.
- [41] Baum, P.; Breuer, M.; Riedle, E.; Steinmeyer, G. *Opt. Lett.* **2006**, *31*, 2220–2222.
- [42] Milota, F.; Mančal, T.; Lukeš, V.; Nemeth, A.; Sperling, J.; Kauffmann, H. F.; Hauer, J. *17th International Conference on Ultrafast Phenomena*; 2010.
- [43] Weiner, A. M. *Rev. Sci. Instrum.* **2000**, *71*, 1929–1960.
- [44] Wefers, M. M.; Nelson, K. A. *IEEE J. Quant. Electron.* **1996**, *32*, 161–172.
- [45] Vaughan, J. C.; Feurer, T.; Stone, K. W.; Nelson, K. A. *Opt. Exp.* **2006**, *14*, 1314–1328.
- [46] Vaughan, J. C.; Hornung, T.; Feurer, T.; Nelson, K. A. *Opt. Lett.* **2005**, *30*, 323–325.
- [47] Trebino, R.; DeLong, K. W.; Fittinghoff, D. N.; Sweetsers, J. N.; Krumbügel, M. A.; Richman, B. A. *Rev. Sci. Instrum.* **1997**, *68*, 3277–3295.
- [48] Lochbrunner, S.; Huppmann, P.; Riedle, E. *Opt. Comm.* **2000**, *184*, 321–328.
- [49] Sweetsers, J. N.; Fittinghoff, D. N.; Trebino, R. *Opt. Lett.* **1997**, *22*, 519–521.

- [50] Selig, U.; Langhojer, F.; Dilmer, F.; Löhrig, T.; Schwarz, C.; Giesecking, B.; Brixner, T. *Opt. Lett.* **2008**, *33*, 2851–2853.
- [51] Nemeth, A.; Sperling, J.; Hauer, J.; Kauffmann, H. F.; Milota, F. *Opt. Lett.* **2009**, *34*, 3301–3303.
- [52] Cowan, M. L.; Ogilvie, J. P.; Miller, R. J. D. *Chem. Phys. Lett.* **2004**, *386*, 184–189.
- [53] Fenna, R. E.; Matthews, B. W. *Nature* **1975**, *258*, 573–577.
- [54] Li, Y. F.; Zhou, W. L.; Blankenship, R. E.; Allen, J. P. *J. Mol. Biol.* **1997**, *271*, 456–471.
- [55] Cho, M. H.; Vaswani, H. M.; Brixner, T.; Stenger, J.; Fleming, G. R. *J. Phys. Chem. B* **2005**, *109*, 10542–10556.
- [56] Perrin, F. *Ann. Phys. Paris* **1932**, *17*, 283–314.
- [57] Knox, R. S. *Photosynth. Res.* **1996**, *48*, 35–39.
- [58] Leegwater, J. A. *J. Phys. Chem.* **1996**, *100*, 14403–14409.
- [59] Savikhin, S.; Buck, D. R.; Struve, W. S. *Chem. Phys.* **1997**, *223*, 303–312.
- [60] Brixner, T.; Stiopkin, I. V.; Fleming, G. R. *Opt. Lett.* **2004**, *29*, 884–886.
- [61] Cho, M. H.; Fleming, G. R. *J. Chem. Phys.* **2005**, *123*, 114506.
- [62] Joo, T.; Jia, Y. W.; Fleming, G. R. *Opt. Lett.* **1995**, *20*, 389–391.
- [63] Lepetit, L.; Chériaux, G.; Joffre, M. *J. Opt. Soc. Am.* **1995**, *12*, 2467–2474.
- [64] Potts, D.; Kunis, S. *SIAM J. Sci. Comput.* **2007**, *29*, 1403–1419.
- [65] Frigo, M.; Johnson, S. G. *Proc. IEEE* **2005**, *93*, 216–231.
- [66] Abramavicius, D.; Valkunas, L.; van Grondelle, R. *Phys. Chem. Chem. Phys.* **2004**, *6*, 3097–3105.
- [67] Renger, T.; May, V.; Kuhn, O. *Phys. Rep.* **2001**, *343*, 138–254.
- [68] Jang, S. J.; Newton, M. D.; Silbey, R. J. *Phys. Rev. Lett.* **2004**, *92*, 9312–9323.
- [69] Novoderezhkin, V.; Wendling, M.; van Grondelle, R. *J. Phys. Chem. B* **2003**, *107*, 11534–11548.
- [70] Vulto, S. I. E.; de Baat, M. A.; Neerken, S.; Nowak, F. R.; van Amerongen, H.; Amez, J.; Aartsma, T. J. *J. Phys. Chem. B* **1999**, *103*, 8153–8161.

- [71] Dreyer, J.; Moran, A. M.; Mukamel, S. *Bull. Korean Chem. Soc.* **2003**, *24*, 1091–1096.
- [72] Hochstrasser, R. M. *Chem. Phys.* **2001**, *266*, 273–284.
- [73] Kempe, J. *Contemp. Phys.* **2003**, *44*, 307–327.
- [74] Grover, L. K. *Phys. Rev. Lett.* **1997**, *79*, 325–328.
- [75] Novoderezhkin, V. I.; Palacios, M. A.; van Amerongen, H.; van Grondelle, R. *J. Phys. Chem. B* **2005**, *109*, 10493–10504.
- [76] Ruban, A. V.; Berera, R.; Ilioaia, C.; van Stokkum, I. H. M.; Kennis, J. T. M.; Pascal, A. A.; van Amerongen, H.; Robert, B.; Horton, P.; van Grondelle, R. *Nature* **2007**, *450*, 575–578.
- [77] Ahn, T. K.; Avenson, T. J.; Ballottari, M.; Cheng, Y.-C.; Niyogi, K. K.; Bassi, R.; Fleming, G. R. *Science* **2008**, *320*, 794–797.
- [78] Linnanto, J.; Martiskainen, J.; Lehtovuori, V.; Ihalainen, J.; Kananavicius, R.; Barbato, R.; Korppi-Tommola, J. *Photosynth. Res.* **2006**, *87*, 267–279.
- [79] Plenio, M. B.; Huelga, S. F. *New J. Phys.* **2008**, *10*, 113019.
- [80] Olaya-Castro, A.; Lee, C. F.; Olsen, F. F.; Johnson, N. F. *Phys. Rev. B* **2008**, *78*, 7.
- [81] Caffarri, S.; Croce, R.; Breton, J.; Bassi, R. *J. Biol. Chem.* **2001**, *276*, 35924–35933.
- [82] Hybl, J. D.; Ferro, A. A.; Jonas, D. M. *J. Chem. Phys.* **2001**, *115*, 6606–6622.
- [83] Frähmcke, J. S.; Walla, P. J. *Chem. Phys. Lett.* **2006**, *430*, 397–403.
- [84] Liu, Z. F.; Yan, H. C.; Wang, K. B.; Kuang, T. Y.; Zhang, J. P.; Gui, L. L.; An, X. M.; Chang, W. R. *Nature* **2004**, *428*, 287–292.
- [85] Ge, N. H.; Zanni, M. T.; Hochstrasser, R. M. *J. Phys. Chem. A* **2002**, *106*, 962–972.
- [86] Yu, Z. G.; Berding, M. A.; Haobin, W. *Phys. Rev. E* **2008**, *78*, 050902.
- [87] Collini, E.; Scholes, G. D. *Science* **2009**, *323*, 369–373.
- [88] Ishizaki, A.; Fleming, G. R. *J. Chem. Phys.* **2009**, *130*, 234111.
- [89] van Grondelle, R.; Novoderezhkin, V. I. *Phys. Chem. Chem. Phys.* **2006**, *8*, 793–807.

- [90] Renger, T.; Marcus, R. A. *J. Chem. Phys.* **2002**, *116*, 9997–10019.
- [91] Renger, T.; Trostmann, I.; Theiss, C.; Madjet, M. E.; Richter, M.; Paulsen, H.; Eichler, H. J.; Knorr, A.; Renger, G. *J. Phys. Chem. B* **2007**, *111*, 10487–10501.
- [92] Dall’Osto, L.; Caffarri, S.; Bassi, R. *Plant Cell* **2005**, *17*, 1217–1232.
- [93] Nielsen, M. A.; Chuang, I. L. *Quantum Computation and Quantum Information*; Cambridge University Press: Cambridge, 2000.
- [94] Fuß, W.; Haas, Y.; Zilberg, S. *Chem. Phys.* **2000**, *259*, 273–295.
- [95] Niedzwiedzki, D.; Kosciielecki, J. F.; Cong, H.; Sullivan, J. O.; Gibson, G. N.; Birge, R. R.; Frank, H. A. *J. Phys. Chem. B* **2007**, *111*, 5984–5998.
- [96] Christensson, N.; Milota, F.; Nemeth, A.; Sperling, J.; Kauffmann, H. F.; Pullerits, T.; Hauer, J. *J. Phys. Chem. B* **2009**, *113*, 16409–16419.
- [97] Wohlleben, W.; Buckup, T.; Hashimoto, H.; Cogdell, R. J.; Herek, J. L.; Motzkus, M. *J. Phys. Chem. B* **2004**, *108*, 3320–3325.
- [98] Larsen, D. S.; Papagiannakis, E.; Van Stokkum, I. H. M.; Vengris, M.; Kennis, J. T. M.; Van Grondelle, R. *Chem. Phys. Lett.* **2003**, *381*, 733–742.
- [99] Cho, M. *Two-Dimensional Optical Spectroscopy*; CRC Press: Boca Raton, FL, 2009.
- [100] Sugisaki, M.; Fujiwara, M.; Nair, S. V.; Ruda, H. E.; Cogdell, R. J.; Hashimoto, H. *Phys. Rev. B* **2009**, *80*, 035118.
- [101] Hauer, J.; Buckup, T.; Motzkus, M. *Chem. Phys.* **2008**, *350*, 220–229.
- [102] Ostroumov, E.; Müller, M. G.; Marian, C. M.; Kleinschmidt, M. K.; Holzwarth, A. R. *Phys. Rev. Lett.* **2009**, *103*, 108302.
- [103] Domcke, W., Yarkony, D. R., Köppel, H., Eds. *Conical Intersections: Electronic Structure, Dynamics & Spectroscopy*; Advanced Series in Physical Chemistry; World Scientific Publishing Co. Pte. Ltd.: Singapore, 2004; Vol. 15.
- [104] Christensson, N.; Polívka, T.; Yartsev, A.; Pullerits, T. *Phys. Rev. B* **2009**, *79*, 245118.
- [105] Pang, Y.; Fleming, G. R. *Phys. Chem. Chem. Phys.* **2010**, *12*, 6782–6788.